

A HYBRID-MIXED FINITE ELEMENT METHOD FOR SINGLE-PHASE Darcy FLOW IN FRACTURED POROUS MEDIA

GUOSHENG FU AND YANG YANG

ABSTRACT. We present a hybrid-mixed finite element method for a novel hybrid-dimensional model of single-phase Darcy flow in a fractured porous media. In this model, the fracture is treated as an $(d - 1)$ -dimensional interface within the d -dimensional fractured porous domain, for $d = 2, 3$. Two classes of fracture are distinguished based on the permeability magnitude ratio between the fracture and its surrounding medium: when the permeability in the fracture is (significantly) larger than in its surrounding medium, it is considered as a *conductive* fracture; when the permeability in the fracture is (significantly) smaller than in its surrounding medium, it is considered as a *blocking* fracture. The conductive fractures are treated using the classical hybrid-dimensional approach of the interface model where pressure is assumed to be continuous across the fracture interfaces, while the blocking fractures are treated using the recent Dirac- δ function approach where normal component of Darcy velocity is assumed to be continuous across the interface. Due to the use of Dirac- δ function approach for the blocking fractures, our numerical scheme allows for nonconforming meshes with respect to the blocking fractures. This is the major novelty of our model and numerical discretization. Moreover, our numerical scheme produces locally conservative velocity approximations and leads to a symmetric positive definite linear system involving pressure degrees of freedom on the mesh skeleton only. The performance of the proposed method is demonstrated by various benchmark test cases in both two- and three-dimensions. Numerical results indicate that the proposed scheme is highly competitive with existing methods in the literature.

1. INTRODUCTION

Numerical simulations of single- and multi-phase flows in porous media have many applications in contaminant transportation, oil recovery and underground radioactive waste deposit. Due to the highly conductive and blocking fractures in the porous media underground, it is still challenging to construct accurate numerical approximations [1, 2, 3].

There are several commonly used mathematical models for simulating flows in porous media with conductive fractures, such as the dual porosity model [4, 5, 6], single porosity model [7], traditional discrete fracture model (DFM) [8, 9, 10, 11, 12, 13, 14], embedded DFM (EDFM) [15, 16, 17, 18, 19, 20, 21], the interface models [22, 23, 24, 25] and extended finite element DFM (XDFM) based on the interface models [26, 27, 28, 29, 30], finite element method based on Lagrange multipliers [31, 32, 33], etc. Among the above methods, the traditional DFM and the interface models have been intensively studied in the past decades.

The DFM is based on the principle of superposition. It uses a hybrid dimensional representation of the Darcy's law, and treats the fractures as lower dimensional entries, with the thickness of the fracture as the dimensional homogeneity factor. The first DFM was introduced by Noorishad and Mehran [8] in 1982 for single phase flows. Later, Baca et al. [9] considered the heat and solute transport in fractured media. Subsequently, several significant numerical methods were applied to the DFM, such as the finite element methods [10, 11, 12, 13, 14], vertex-centered finite volume methods [34, 35, 36, 37], cell-centered finite volume methods [38, 39, 40, 41, 42], mixed finite

2020 *Mathematics Subject Classification.* 65N30, 65N12, 76S05, 76D07.

Key words and phrases. Hybrid-mixed finite element method; fractured porous media, hybrid-dimensional model.

G. Fu was partially supported by the NSF grant DMS-2012031. Y. Yang was partially supported by the NSF grant DMS-1818467.

element methods [43, 44, 45, 46, 47, 48, 49, 50], discontinuous Galerkin methods [51]. All the above works are limited on conforming meshes, i.e. the fractures are aligned with the interfaces of the background matrix cells. Therefore, it may suffer from low quality cells. Recently, Xu and Yang introduced the line Dirac- δ functions [52] to represent the conductive fractures and reinterpreted the DFM (RDFM) on nonconforming meshes. The basic idea is to superpose the conductivity of the fracture to that of the matrix. The main contribution in [52] is to explicitly represent the DFM introduced in [12] as a scalar partial differential equation. Therefore, with suitable numerical discretizations, such as the discontinuous Galerkin method, the RDFM can be applied to arbitrary meshes. To demonstrate that the RDFM is exactly the traditional DFM if the mesh is conforming, in [52] only finite element methods were considered. Therefore, local mass conservation was missing. Later, the enriched Galerkin and interior penalty discontinuous Galerkin methods were applied to RDFM in [53] and the contaminant transportation was also simulated.

Different from the traditional DFM, the interface model [22, 23, 24, 25] explicitly represent the fractures as interfaces of the porous media. Then the governing equation of the flow in the lower dimensional fracture was constructed. In the interface model, the matrix and fractures are considered as two systems, and the communication between them was given as the jump the normal velocity along the fractures. Therefore, different from RDFM, the interface model, though hanging nodes are allowable, cannot be applied to structured meshes and the fracture must be aligned with the interfaces of the meshes for the matrix. To fixed this limitation, the XDFM was proposed [26, 27, 28, 29, 30]. However, these methods may increase the degrees of freedom (DOFs) significantly, and can hardly be applied to fracture networks with high geometrical complexity [54]. As an alternative, the CutFEM [55] can be applied to non-conforming meshes. It couples the fluid flow in all lower dimensional manifolds. However, this method requires the fractures to cut the domain into completely disjoint subdomains, thus it is not applicable for media with complicated fractures.

Most of the above ideas work for problems with conductive fractures. However, if the media contains blocking fractures, most methods may not be suitable. To fix this gap, the projection-based EDFM (pEDFM) was introduced in [18, 56]. The effective flow area between adjacent matrix grids is computed as the difference between the original interface area and the projected area of the fracture segment. It will be zero if the fracture fully penetrates through the matrix cell. Olorode et al. [57] extended the pEDFM into three-dimensional compositional simulation of fractured reservoirs. However the pEDFM still cannot describe the complex multiphase flow behavior in the matrix blocks within barrier fractures. Another approach is to follow the interface model introduced in [58, 59, 60, 61]. However, as demonstrated above, the interface model can only handle hanging nodes, and the fractures must align with the interfaces of the background mesh. Recently, Xu and Yang extended the RDFM [52, 53] to problems with blocking fractures in [62]. The basic idea is to apply Ohm's law and superpose the resistance (the reciprocal of the permeability) of the blocking fracture to that of the matrix. Then a modified partial differential equation system was introduced and the local discontinuous Galerkin methods with suitable penalty were perfectly applied. If the problems contains only blocking fractures, the mixed finite element methods can easily be combined with RDFM.

In this paper, we combine the ideas in [22] and [62] to propose a novel model for single phase flows with both conductive and blocking fractures. In particular, the conductive fractures are modeled by using the interface model [22] where pressure continuity is enforced across the conductive fractures, and the blocking fractures are modelled as resistance terms involving Dirac- δ functions following the main idea in [62]. The separate treatment of conductive and blocking fractures, and the seamless combination of the conductive fracture interface model and the blocking fracture Dirac- δ function approach is the major novelty of our proposed model. We further discretize this new model using a hybrid-mixed finite element method, which produces locally conservative velocity approximations and leads to a symmetric positive definite linear system with globally coupled degrees of freedom

(DOFs) only those of pressure on the mesh skeletons. Moreover, due to the use of Dirac- δ function approach for blocking fractures, the method does not require any mesh conformity with respect to the blocking fractures, which is the major novelty of our proposed scheme. We believe our approach is the simplest non-conforming mesh approach to blocking fractures that still yield locally conservative velocity approximations. We note that mesh conformity with respect to the conductive fractures is still required for our method, which is typical for interface models. We numerically demonstrate that our hybrid-mixed finite element scheme is highly competitive both in terms of computational efficiency and accuracy. We finally emphasize that the proposed hybrid-mixed formulation is different from the mixed method in [60] due to the use of different model for the interface conditions. We believe that our model is significantly simpler for complex fracture networks since we only use one matrix domain and one (codimension 1) conductive fracture domain throughout, while the mixed method formulation [60] needs to split the matrix and fracture domains into multiple disjoint sub-domains and require the modeling of codimension 1-3 fracture flows, which might be very tedious to perform for complex fracture networks.

The rest of the paper is organized as follows. In Section 2, we present the hybrid-dimensional model under consideration. We then formulate in Section 3 the hybrid-mixed finite element discretization of the model proposed in Section 2. Numerical results for various benchmark test cases are presented in Section 4. We conclude in Section 5.

2. THE HYBRID-DIMENSIONAL MODEL

2.1. Notation. We consider a bounded open domain $\Omega_m \subset \mathbb{R}^d$, $d = 2, 3$, which contains several $(d-1)$ -dimensional conductive or blocking fractures. For simplicity, the fractures are assumed to be hyperplanes with smooth boundaries. We denote Ω_c as the $(d-1)$ -dimensional open set containing all the conductive fractures, and Ω_b as the set containing all the blocking fractures. Assume the $(d-1)$ -dimensional domain boundary $\partial\Omega_m = \Gamma_D \cup \Gamma_N$, with $\Gamma_D \cap \Gamma_N = \emptyset$. Furthermore, we denote the following sets of $(d-2)$ -dimensional boundaries (intersections) associated with the set of conductive fractures Ω_c :

- Γ_{cc} is the set containing the intersections among conductive fractures.
- Γ_{cb} is the set containing the intersections between 2 conductive and blocking fractures.
- Γ_{cm} is the set containing the intersections between conductive fractures and domain boundary $\partial\Omega_m$, which is further split to $\Gamma_{cm} = \Gamma_{cm}^N \cup \Gamma_{cm}^D$ with $\Gamma_{cm}^N \in \Gamma_N$ and $\Gamma_{cm}^D \in \Gamma_D$.
- Γ_{ci} is the boundary of Ω_c that does not intersect with the domain boundary $\partial\Omega_m$.

We set $\Gamma_c = \Gamma_{cc} \cup \Gamma_{cb} \cup \Gamma_{cm} \cup \Gamma_{ci}$ as the collections of all intersections of Ω_c . An illustration of a typical hybrid-dimensional domain in two-dimensions is given in Figure 1.

We denote \mathbf{n}_Γ as a uniquely oriented unit normal vector on a $(d-1)$ -dimensional interface/boundary Γ , and denote $\boldsymbol{\eta}_\Gamma$ as the *in-plane* unit (outer) normal vector on the $(d-2)$ dimensional boundary $\partial\Gamma$ of Γ , see Figure 2.

Let ϵ be the thickness of the fractures, which is assumed to be a small positive constant for simplicity. Let \mathbb{K}_m be the permeability tensor of the domain excluding the fractures $\Omega_m \setminus \{\Omega_c \cup \Omega_b\}$, $K_b \ll \mathbb{K}_m$ be the (scalar) permeability in the normal direction of blocking fractures Ω_b , and $\mathbb{K}_c \gg \mathbb{K}_m$ be the permeability tensor in the tangential direction of the conductive fractures Ω_c .

2.2. The hybrid-dimensional flow model. The following hybrid-dimensional model is a combination of the conductive fracture treatment in [22] and blocking fracture treatment in [62]. In the bulk domain $\Omega_m \setminus \Omega_c$ excluding conductive fractures, we use the following barrier model:

$$(\mathbb{K}_m^{-1} + \frac{\epsilon}{K_b} \delta_{\Omega_b} \mathbf{n}_{\Omega_b} \otimes \mathbf{n}_{\Omega_b}) \mathbf{u} = -\nabla p, \quad \text{in } \Omega_m \setminus \Omega_c, \quad (1a)$$

$$\nabla \cdot \mathbf{u} = f, \quad \text{in } \Omega_m \setminus \Omega_c, \quad (1b)$$

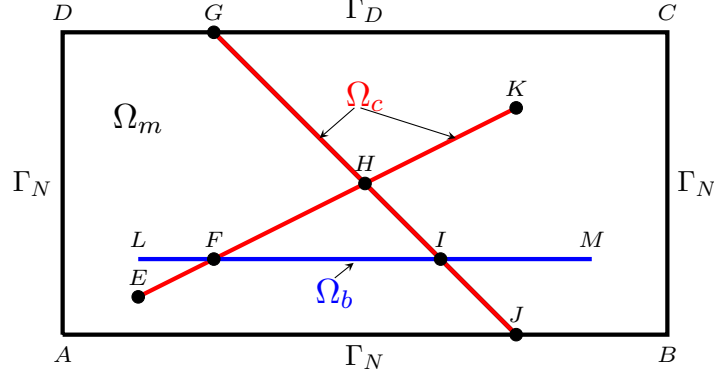


FIGURE 1. A typical two dimensional fractured domain Ω_m (the rectangular domain). The domain boundary $\Gamma_D = \{CD\}$, $\Gamma_N = \{AB\} \cup \{BC\} \cup \{AD\}$, where $\{AB\}$ denotes the line segment connecting nodes A and B . Here $\Omega_c = \{EK\} \cup \{JG\}$, $\Omega_b = \{LM\}$, $\Gamma_{cc} = H$, $\Gamma_{cb} = F \cup I$, $\Gamma_{cm}^D = G$, $\Gamma_{cm}^N = J$, and $\Gamma_{ci} = E \cup K$.

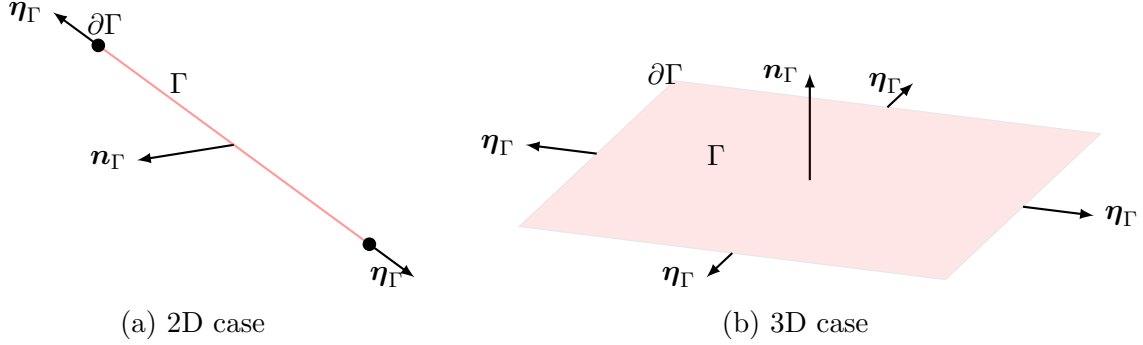


FIGURE 2. Normal direction \mathbf{n}_Γ and in-plane normal direction $\boldsymbol{\eta}_\Gamma$ for a $(d-1)$ -dimensional interface/boundary Γ . Left: $d=2$, Γ is a line segment. Right: $d=3$, Γ is a planar quadrangle.

where \mathbf{u} is the Darcy velocity, p is the pressure, f is the volume source term, δ_{Ω_b} is the Dirac- δ function that takes values ∞ on the blocking fractures Ω_b and zero elsewhere, and \mathbf{n}_{Ω_b} is the unit normal vector on Ω_b . Within the conductive fractures excluding intersections $\Omega_c \setminus \Gamma_c$, we use the following $(d-1)$ -dimensional Darcy's law:

$$(\epsilon \mathbb{K}_c)^{-1} \mathbf{u}_c = -\nabla_\Gamma p_c, \quad \text{in } \Omega_c \setminus \Gamma_c, \quad (1c)$$

$$\nabla_\Gamma \cdot \mathbf{u}_c = \llbracket \mathbf{u} \rrbracket, \quad \text{in } \Omega_c \setminus \Gamma_c, \quad (1d)$$

where \mathbf{u}_c is the (tangential) Darcy velocity in the conductive fractures, p_c is the associated pressure, and the velocity jump $\llbracket \mathbf{u} \rrbracket = (\mathbf{u}^+ - \mathbf{u}^-) \cdot \mathbf{n}_\Gamma$ represents the mass exchange between the conductive fractures and the surrounding media, where $\mathbf{u}^\pm(\mathbf{x}) = \lim_{\tau \rightarrow 0^\pm} \mathbf{u}(\mathbf{x} - \tau \mathbf{n}_\Gamma)$ for all $\mathbf{x} \in \Omega_c$ is the bulk Darcy velocity evaluated on one side of the conductive fractures. Moreover, ∇_Γ and $\nabla_\Gamma \cdot$ are the usual surface gradient and surface divergence operators. The above hybrid-dimensional system

is closed with the following set of boundary/interface conditions:

$$p = p_D, \quad \text{on } \Gamma_D, \quad (1e)$$

$$\mathbf{u} \cdot \mathbf{n} = q_N, \quad \text{on } \Gamma_N, \quad (1f)$$

$$p = p_c, \quad \text{on } \Omega_c, \quad (1g)$$

$$[[\mathbf{u}_c]] = 0, \quad \text{on } \Gamma_{cc}, \quad (1h)$$

$$p_c = p_D, \quad \text{on } \Gamma_{cm}^D, \quad (1i)$$

$$\mathbf{u}_c \cdot \boldsymbol{\eta}_\Gamma = 0, \quad \text{on } \Gamma_{cb} \cup \Gamma_{cm}^N \cup \Gamma_{ci}, \quad (1j)$$

where (1g) ensures continuity of bulk pressure across conductive fractures, the no-flow boundary condition in (1j) is imposed on the intersections Γ_{cb} , Γ_{cm}^N and Γ_{ci} , and the jump term in (1h) is

$$[[\mathbf{u}_c]]|_e := \sum_{\Gamma \subset \Omega_c \setminus \Gamma_c, e \in \bar{\Gamma}} \mathbf{u}_c|_\Gamma \cdot \boldsymbol{\eta}_\Gamma, \quad \forall e \in \Gamma_{cc},$$

which represents mass conservation along intersections Γ_{cc} . Note in particular that each conductive fracture containing the intersection e appears exactly twice in the above summation, and the in-plane normal velocity on the fracture is allowed to be discontinuous along the intersection e . For example, the jump $[[\mathbf{u}_c]]_H$ at node H in the configuration in Figure 1 is

$$[[\mathbf{u}_c]]_H := \sum_{\Gamma \in \{\{EH\}, \{HK\}, \{GH\}, \{HJ\}\}} \mathbf{u}_c|_\Gamma \cdot \boldsymbol{\eta}_\Gamma.$$

We note that in the above model (1), the flow in the tangential direction in the blocking fractures is completely ignored as the permeability therein is much smaller than that of the surroundings, on the other hand, the flow in the normal direction is ignored on conductive fractures by the pressure continuity condition (1g) since the permeability is much larger than that of the surroundings and the fluid has a tendency to flow along the tangential direction therein.

2.3. The hybrid-dimensional transport model. We now consider a scalar quantity c that is transported through the porous medium subject to the velocity fields in the flow model (1). Here c usually represents the concentration of a generic passive tracer. Similar to the flow treatment in the previous subsection, transport inside the blocking fractures is ignored. The concentrations c in the matrix and c_c in the conductive fractures are governed by the following advection equations, see e.g. [63, 64, 25],

$$\phi_m \frac{\partial c}{\partial t} + \nabla \cdot (\mathbf{u}c) = cf, \quad \text{in } \Omega_m \setminus \Omega_c \times (0, T], \quad (2a)$$

$$\epsilon \phi_c \frac{\partial c_c}{\partial t} + \nabla_\Gamma \cdot (\mathbf{u}_c c_c) - [[c\mathbf{u}]] = 0, \quad \text{in } \Omega_c \times (0, T], \quad (2b)$$

with the following initial, interface, and boundary conditions

$$c = c_c \quad \text{on } \Omega_c \times (0, T], \quad (2c)$$

$$c = c_0 \quad \text{on } \Omega \times 0, \quad c_c = c_{c,0} \quad \text{on } \Omega_c \times 0, \quad (2d)$$

$$c = c_B \quad \text{on } \partial\Omega_{in} \times (0, T], \quad c_c = c_{c,B} \quad \text{on } \Gamma_{in} \times (0, T], \quad (2e)$$

where $\{\phi_m, c_0, c_B, \partial\Omega_{in}\}$ and $\{\phi_c, c_{c,0}, c_{c,B}, \Gamma_{in}\}$ represent the {porosity, initial concentration, inflow concentration, and inflow boundary} in the matrix and conductive fractures, respectively. Observe that concentration continuity (2c) across the conductive fractures are enforced in the model (2).

3. THE HYBRID-MIXED FINITE ELEMENT METHOD

3.1. Preliminaries. Let $\mathcal{T}_h := \{K\}$ be a conforming simplicial triangulation of the domain Ω_m . Let \mathcal{E}_h be the collections of $(d-1)$ -dimensional facets (edges for $d=2$, faces for $d=3$) of Ω_m . Assume the mesh is fully fitted with respect to the conductive fractures, i.e., $\mathcal{T}_h^c := \Omega_c \cap \mathcal{E}_h$ is a $(d-1)$ -dimensional simplicial triangulation of the domain Ω_c . Here the mesh \mathcal{T}_h is allowed to be unfitted with respect to the blocking fractures. Moreover, we denote \mathcal{E}_h^c as the collection of $(d-2)$ -dimensional facets of \mathcal{T}_h^c (vertices for $d=2$, edges for $d=3$).

We use the lowest-order hybrid-mixed finite element methods to discretize the model (1). The following finite element spaces will be needed:

$$\mathbf{V}_h := \{\mathbf{v} \in [L^2(\mathcal{T}_h)]^d : \mathbf{v}|_K \in RT_0(K), \quad \forall K \in \mathcal{T}_h\}, \quad (3a)$$

$$W_h := \{w \in L^2(\mathcal{T}_h) : w|_K \in P_0(K), \quad \forall K \in \mathcal{T}_h\}, \quad (3b)$$

$$M_h := \{\mu \in L^2(\mathcal{E}_h) : \mu|_F \in P_0(F), \quad \forall F \in \mathcal{E}_h\}, \quad (3c)$$

$$\mathbf{V}_h^c := \{\mathbf{v}_c \in [L^2(\mathcal{T}_h^c)]^d : \mathbf{v}|_F \in RT_0(F), \quad \forall F \in \mathcal{T}_h^c\}, \quad (3d)$$

$$M_h^c := \{\mu \in L^2(\mathcal{E}_h^c) : \mu|_E \in P_0(E), \quad \forall E \in \mathcal{E}_h^c\}, \quad (3e)$$

where $RT_0(S)$ is the Raviart-Thomas space of lowest order on a simplex S , and $P_0(S)$ is the space of constants.

We denote the following inner products:

$$\begin{aligned} (\phi, \psi)_{\mathcal{T}_h} &:= \sum_{K \in \mathcal{T}_h} \int_K \phi \psi \, dx, & \langle \phi, \psi \rangle_{\partial \mathcal{T}_h} &:= \sum_{K \in \mathcal{T}_h} \int_{\partial K} \phi \psi \, ds, \\ \langle \phi, \psi \rangle_{\mathcal{T}_h^c} &:= \sum_{F \in \mathcal{T}_h^c} \int_F \phi \psi \, ds, & [\phi, \psi]_{\partial \mathcal{T}_h^c} &:= \sum_{F \in \mathcal{T}_h^c} \int_{\partial F} \phi \psi \, dr, \end{aligned}$$

where dx is for d -dimensional integration, ds is for $(d-1)$ -dimensional integration, and dr is for $(d-2)$ -dimensional integration. When $d=2$, $\int_{\partial F} \phi \psi \, dr$ is simply the sum of point evaluations at the two end points of a line segment F .

3.2. The hybrid-mixed method for the flow model. The hybrid-mixed method for the hybrid-dimensional model (1) is given as follows: Find $(\mathbf{u}_h, p_h, \hat{p}_h, \mathbf{u}_h^c, \hat{p}_h^c) \in \mathbf{V}_h \times W_h \times M_h \times \mathbf{V}_h^c \times M_h^c$ with $\hat{p}_h|_{\Gamma_D} = \mathbb{P}_0(p_D)$ and $\hat{p}_h^c|_{\Gamma_{cm}^D} = \mathbb{P}_0(p_D)$, where \mathbb{P}_0 denotes the projection onto piecewise constants, such that

$$(\mathbb{K}_m^{-1} \mathbf{u}_h, \mathbf{v}_h)_{\mathcal{T}_h} + \int_{\Omega_b} \frac{\epsilon}{K_b} (\mathbf{u}_h \cdot \mathbf{n})(\mathbf{v}_h \cdot \mathbf{n}) \, ds - (p_h, \nabla \cdot \mathbf{v}_h)_{\mathcal{T}_h} + \langle \hat{p}_h, \mathbf{v}_h \cdot \mathbf{n} \rangle_{\partial \mathcal{T}_h} = 0, \quad (4a)$$

$$(\nabla \cdot \mathbf{u}_h, q_h)_{\mathcal{T}_h} - (f, q_h)_{\mathcal{T}_h} = 0, \quad (4b)$$

$$-\langle \mathbf{u}_h \cdot \mathbf{n}, \hat{q}_h \rangle_{\partial \mathcal{T}_h} + \langle \nabla_{\Gamma} \cdot \mathbf{u}_h^c, \hat{q}_h \rangle_{\mathcal{T}_h^c} + \int_{\Gamma_N} q_N \hat{q}_h \, ds = 0, \quad (4c)$$

$$\langle (\epsilon \mathbb{K}_c)^{-1} \mathbf{u}_h^c, \mathbf{v}_h^c \rangle_{\mathcal{T}_h^c} - \langle \hat{p}_h, \nabla_{\Gamma} \cdot \mathbf{v}_h^c \rangle_{\mathcal{T}_h^c} + [\hat{p}_h^c, \mathbf{v}_h^c \cdot \boldsymbol{\eta}]_{\partial \mathcal{T}_h^c} + \int_{\Gamma_{cb}} \alpha (\epsilon \mathbb{K}_c)^{-1} (\mathbf{u}_h^c \cdot \boldsymbol{\eta})(\mathbf{v}_h^c \cdot \boldsymbol{\eta}) \, dr = 0, \quad (4d)$$

$$-[\mathbf{u}_h^c \cdot \boldsymbol{\eta}, \hat{q}_h^c]_{\partial \mathcal{T}_h^c} = 0, \quad (4e)$$

for all $(\mathbf{v}_h, q_h, \hat{q}_h, \mathbf{v}_h^c, \hat{q}_h^c) \in \mathbf{V}_h \times W_h \times M_h \times \mathbf{V}_h^c \times M_h^c$ with $\hat{q}_h|_{\Gamma_D} = \hat{q}_h^c|_{\Gamma_{cm}^D} = 0$, where $\alpha > 0$ is a penalty parameter for the implementation of the no-flow boundary condition (1j) on Γ_{cb} . In our numerical implementation, we take $\alpha = 10^6$.

We show that the scheme (4) is formally consistent with the hybrid-dimensional model (1):

- (1) Equation (4a) is a discretization of the Darcy's law (1a) in the bulk using integration-by-parts and the following property of Dirac- δ function:

$$\int_{\Omega_m} \delta_{\Omega_b} \phi dx = \int_{\Omega_b} \phi ds.$$

- (2) Equation (4b) is the discretization of mass conservation (1b) in the bulk.
 (3) Equation (4c) simultaneously enforces (i) the continuity of normal velocity $\mathbf{u}_h \cdot \mathbf{n}$ across interior element boundaries $\mathcal{E}_h \setminus (\mathcal{T}_h^c \cup \Gamma_N)$, (ii) the boundary condition (1f) on Γ_N , and (iii) mass conservation (1d) within the conductive fractures in \mathcal{T}_h^c .
 (4) Equation (4d) is a discretization of the Darcy's law (1c) on the conductive fractures \mathcal{T}_h^c , where the pressure continuity condition (1h) is also strongly enforced as \hat{p}_h both represents the bulk pressure on the element boundary \mathcal{E}_h and the pressure within the conductive fracture \mathcal{T}_h^c . Moreover, the last term in (4d) is a penalty formulation of the no-flow boundary condition (1j) on Γ_{cb} . Note that Γ_{cb} is allowed to be not aligned with the facets of \mathcal{T}_h^c .
 (5) Equation (4e) is a transmission condition that simultaneously enforces (i) continuity of in-plane normal velocity $\mathbf{u}_h^c \cdot \boldsymbol{\eta}$ on interior facets $E_h^c \setminus \{\Gamma_{cc} \cup \Gamma_{cm}^N \cup \Gamma_{ci}\}$, (ii) the mass conservation (1h) on the intersections Γ_{cc} (iii) the no-flow boundary condition (1j) on Γ_{cm}^N and Γ_{ci} .
 (6) The Dirichlet boundary condition (1e) and (1i) are imposed strongly through the corresponding degrees of freedom (DOFs) on \hat{p}_h and \hat{p}_h^c , respectively.

The following result further shows that the scheme (4) is well-posed.

Theorem 3.1. *Assume the measure of the Dirichlet boundary Γ_D is not empty, then the solution to the scheme (4) exists and is unique.*

Proof. Since the equations in (4) leads to a square linear system, we only need to show uniqueness. Now we assume the source terms in (4) vanishes, i.e., $f = p_D = g_N = 0$. Taking test function to be the same as trial functions in (4) and adding, we get

$$(\mathbb{K}_m^{-1} \mathbf{u}_h, \mathbf{u}_h)_{\mathcal{T}_h} + \int_{\Omega_b} \frac{\epsilon}{K_b} (\mathbf{u}_h \cdot \mathbf{n})^2 ds + \langle (\epsilon \mathbb{K}_c)^{-1} \mathbf{u}_h^c, \mathbf{u}_h^c \rangle_{\mathcal{T}_h^c} = 0.$$

Hence, $\mathbf{u}_h = \mathbf{u}_h^c = 0$. Since $\mathbf{u}_h = 0$, the inf-sup stability of the RT_0 - P_0 finite element pair implies that $p_h = \hat{p}_h = C$ from (4a) where C is a constant. Since Γ_D is not empty and $p_D = 0$, we get the constant $C = 0$. Finally, restricting equation (4d) to a single element $F \in \mathcal{T}_h^c$ and using the fact that $\mathbf{u}_h^c = 0$ and $\hat{p}_h = 0$, we get

$$\int_{\partial F} \hat{p}_h^c \mathbf{v}_h^c \cdot \boldsymbol{\eta} ds = 0, \quad \forall \mathbf{v}_h^c \in RT_0(F),$$

which then implies that $\hat{p}_h^c = 0$. This completes the proof. \square

3.3. Static condensation and linear system solver. The linear system (4) can be efficiently solved via static condensation, where the DOFs for \mathbf{u}_h , p_h , and \mathbf{u}_h^c can be locally eliminated, resulting in a coupled global linear system for the DOFs for \hat{p}_h and \hat{p}_h^c , which is symmetric and positive definite. Efficient linear system solvers for the resulting condensed system is an interesting topic where one could design efficient decoupling algorithms or robust monolithic preconditioners. Here we simply use a sparse direct solver in the computation and postpone the detailed study of linear system solvers to our future work.

3.4. Local pressure postprocessing. We use the following well-known local (piecewise linear) pressure postprocessing to improve the accuracy of pressure approximation in the bulk: find

$$p_h^* \in W_h^* := \{w \in L^2(\mathcal{T}_h) : w|_K \in P_1(K), \quad \forall K \in \mathcal{T}_h\},$$

where $P^1(K)$ is the space of linear polynomials on element K , such that

$$(\nabla p_h^*, \nabla q_h^*)_{\mathcal{T}_h} = -(\mathbb{K}_m^{-1} \mathbf{u}_h, \nabla q_h^*)_{\mathcal{T}_h}, \quad (5a)$$

$$(p_h^*, 1)_{\mathcal{T}_h} = (p_h, 1)_{\mathcal{T}_h}, \quad (5b)$$

for all $q_h^* \in W_h^*$.

3.5. The hybridized finite volume method for the transport model. We consider a standard cell-centered, first-order upwinding finite volume scheme for the transport model (2), coupled with the implicit Euler method for the temporal discretization. We hybridize the cell-centered finite volume scheme so that the coupled unknowns live on the mesh skeletons, which simplifies the definition of upwinding fluxes on the conductive fracture interactions (e.g. point H in Figure 1). Hence we use piecewise constant spaces to approximate the matrix concentration $c_h \in W_h$ on the mesh \mathcal{T}_h , the matrix concentration $\hat{c}_h \in M_h$ on the matrix mesh skeleton \mathcal{E}_h , and the fracture concentration $\hat{c}_{c,h} \in M_{c,h}^c$ on the fracture mesh skeleton $\mathcal{E}_{c,h}^c$.

The hybridized finite volume scheme with implicit Euler temporal discretization is given as follows: given data $(c_h^{n-1}, \hat{c}_h^{n-1}) \in W_h \times M_h$ at time t^{n-1} , find $(c_h^n, \hat{c}_h^n, \hat{c}_{c,h}^n) \in W_h \times M_h \times M_{c,h}^c$ at time $t^n := t^{n-1} + \Delta t$ with $\hat{c}_h^n|_{\partial\Omega_{in}} = P_0(c_B(t^n))$ and $\hat{c}_{c,h}^n|_{\Gamma_{in}} = P_0(c_{c,B}(t^n))$ such that

$$\left(\phi_m \frac{c_h^n - c_h^{n-1}}{\Delta t}, d_h \right)_{\mathcal{T}_h} + \langle \mathbf{u}_h \cdot \mathbf{n} \hat{c}_h^{n,*}, d_h \rangle_{\partial\mathcal{T}_h} = (c_h^n f, d_h)_{\mathcal{T}_h}, \quad (6a)$$

$$-\langle \mathbf{u}_h \cdot \mathbf{n} \hat{c}_h^{n,*}, \hat{d}_h \rangle_{\partial\mathcal{T}_h} + \left\langle \epsilon \phi_c \frac{\hat{c}_h^n - \hat{c}_h^{n-1}}{\Delta t}, \hat{d}_h \right\rangle_{\mathcal{T}_h^c} + [\mathbf{u}_h^c \cdot \boldsymbol{\eta} \hat{c}_{c,h}^{n,*}, \hat{d}_h]_{\partial\mathcal{T}_h^c} = 0, \quad (6b)$$

$$[\mathbf{u}_h^c \cdot \boldsymbol{\eta} \hat{c}_{c,h}^{n,*}, \hat{d}_{c,h}]_{\partial\mathcal{T}_h^c} = 0, \quad (6c)$$

for all $(d_h, \hat{d}_h, \hat{d}_{c,h}) \in W_h \times M_h \times M_{c,h}^c$ with $\hat{d}_h|_{\partial\Omega_{in}} = 0$ and $\hat{d}_{c,h}|_{\Gamma_{in}} = 0$, where the upwinding fluxes are given as follows:

$$\hat{c}_h^{n,*}|_{\partial K} = \begin{cases} c_h^n & \text{if } \mathbf{u}_h \cdot \mathbf{n}_K > 0, \\ \hat{c}_h^n & \text{if } \mathbf{u}_h \cdot \mathbf{n}_K \leq 0, \end{cases} \quad (6d)$$

$$\hat{c}_{c,h}^{n,*}|_{\partial F} = \begin{cases} \hat{c}_h^n & \text{if } \mathbf{u}_h^c \cdot \boldsymbol{\eta}_F > 0, \\ \hat{c}_{c,h}^n & \text{if } \mathbf{u}_h^c \cdot \boldsymbol{\eta}_F \leq 0. \end{cases} \quad (6e)$$

3.6. Remarks on the mesh restrictions and comparison with existing methods. The proposed flow and transport solvers (4), (6) require the mesh to be fitted to the conductive fractures, while allowing for an unfitted treatment of the blocking fractures. While the derivation of numerical schemes that work on fully unfitted meshes is beyond the scope of this paper, here we propose a simple mesh postprocessing technique to convert a general unfitted background matrix mesh to an *immersed* mesh that is fitted to all the fractures. Similar immersing mesh techniques were used for interface problems [65, 66, 67, 68]. Below we illustrate the procedure of immersing a single fracture to an unfitted tetrahedral mesh in 3D:

- (i) Represent the fracture geometry as the zero level set of a continuous piecewise linear function ϕ_h on the background mesh. Perturb ϕ_h slightly if necessary to avoid fracture pass through the background mesh nodes.
- (ii) Loop over the background mesh edges, find the cut edges where ϕ_h has opposite sign on the two edge endpoints. For each cut edge, compute the coordinates of the cut vertex v_c where $\phi_h(v_c) = 0$, and add v_c to the mesh nodes.
- (iii) Loop over the background mesh faces, find the cut faces which contains the cut vertices. Order the cut vertices based on their vertex label number. Loop over the cut vertices, for

each (sub-)face that contains the cut vertex, split the (sub-)face by 2 by connecting the cut vertex with the opposite (sub-)face node.

- (iv) Loop over the background mesh elements, find the cut elements which contains the cut vertices. Order the cut vertices based on their vertex label number. Loop over the cut vertices, for each (sub-)element that contains the cut vertex, split the (sub-)element by 2 by connecting the cut vertex with the opposite two (sub-)element nodes that are not aligned with the cut edge.

The above recursive bisection procedure guarantees that the fracture lies on the boundary of the generated immersed mesh. The case with multiply intersecting fractures can be treated by recursion. Here we note that the generated immersed mesh is usually highly anisotropic since the background mesh is completely independent of the fracture configurations. Our numerical results in the next section suggest that the hybrid-mixed method (4) works well on these anisotropic immersed meshes. Typical 2D immersed meshes for complex fracture configurations are given in Figure 11 and Figure 14 below.

We now briefly compare our proposed fractured flow solver (4) with some existing schemes in [69], which were used to solve a series of 4 benchmark problems in 3D fractured porous media flow. Among the 17 schemes in [69, Table 1], 7 were shown to yield no significant deviations for all the tests, see [69, Figure 18], which include the multi-point flux approximation (UiB-MPFA), the lowest order mixed virtual element method (UiB-MVEM), and the lowest order Raviart-Thomas mixed finite element method (UiB-RT0) mainly developed by the research group in the University of Bergen [70, 71, 60], the MPFA scheme (USTUTT-MPFA) and the two-point flux approximation scheme (USTUTT-TPFA_Circ) developed by Flemisch et al. [72], the mimetic finite difference method (LANL-MFD) [73], and the hybrid finite volumes discontinuous hydraulic head method (UNICE_UNIGE-HFV_Disc) developed by Brenner et al. [74]. Among these 7 schemes, the first three schemes use a mixed dimensional interface model that require the modeling of co-dimension 1-3 fractured flows, where the mesh can be non-matching across subdomains, but needs to be geometrically conforming to the fractures. On the other hand, the last four schemes work on a mixed dimensional interface model where only fractured flow in co-dimension 1 were modeled, which require the mesh to be completely conforming to the fractures. All of these schemes yield a locally conservative velocity approximation. We further note that the two methods in [69] that allow for general nonconforming meshes, namely the Lagrange multiplier method [31, 32, 33] and the EDFM method [75], cannot handle blocking fractures and do not provide a locally conservative velocity approximation.

Numerical results of our proposed scheme (4) for the benchmark problems in [69] indicate that our results yield no significant deviations with the above mentioned 7 schemes, see details in the next section. Our scheme also produce a locally conservative velocity approximation, and the resulting linear system after static condensation is a symmetric positive definite (SPD) problem with global unknowns involve pressure DOFs on the mesh skeleton only. The number of the global unknowns of our scheme is roughly N_F , which is the total number of mesh faces, and the average nonzero entries per row in the system matrix is 7 (a pressure DOF on an interior tetrahedral face is connected to 6 neighboring face pressure DOFs). Concerning the computational cost of our scheme, it is more expensive than the TPFA scheme (USTUTT-TPFA_Circ) which lead to an SPD system with roughly N_C cell-wise pressure DOFs and about 5 nonzero entries per row in the system matrix, is slightly less expensive than the cell-based MPFA schemes (UiB-MPFA, USTUTT-MPFA), which lead to SPD systems with roughly N_C cell-wise pressure DOFs and about 20-50 nonzero entries per row in the system matrix, and is significantly cheaper than the schemes UiB-MVEM, UiB-RT0, LANL-MFD, and UNICE_UNIGE-HFV_Disc, which lead to saddle point systems with total number of roughly N_F velocity DOFs and N_C pressure DOFs. Note that $N_F \approx 2N_C$. Hence, our proposed scheme is also highly competitive in terms of computational costs. Another distinctive

advantage of our scheme over these 7 schemes is that the mesh can be completely nonconforming to the blocking fractures.

4. NUMERICS

In this section, we present detailed numerical results for the proposed hybrid-mixed method for the four 2D benchmark test cases in [54] and the four 3D benchmark test cases in [69]. We name the method (4) as HM-DFM since it is a hybrid mixed method for a discrete fracture model. When plotting the pressure or hydraulic head distribution over line segments, we evaluate the second-order postprocessed solution in (5) for the proposed method. The focus of the numerical experiments is on the verification of the accuracy of our proposed flow model (1) and the associated method (4). Hence, we test the flow solver (4) for all the 8 benchmark cases. Meanwhile, we also test the accuracy of velocity approximation by feeding them to the transport problem (2), which is solved using the scheme (6) for three cases, namely Benchmark 2 in 2D, and Benchmark 5/6 in 3D. Furthermore, convergence study via mesh refinements was conducted for Benchmark 2 and Benchmark 6 below.

Our numerical simulations are performed using the open-source finite-element software NGSolve [76], <https://ngsolve.org/>. Jupyter notebooks for reproducing all numerical examples in this section can be found in the git repository <https://github.com/gridfunction/fracturedPorousMedia>. Visualization of meshes for the 3D benchmark examples and interactive contour plots of the pressure/hydraulic head can also be found therein.

4.1. Benchmark 1: Hydrocoin (2D). This example is originally a benchmark for heterogeneous groundwater flow presented in the international Hydrocoin project [77]. A slight modification for the geometry was made in [54, Section 4.1], and we follow the settings therein. In particular, the bulk domain is a polygon with vertices $A = (0, 150)$, $B = (400, 100)$, $C = (800, 150)$, $D = (1200, 100)$, $E = (1600, 150)$, $F = (1600, -1000)$, $G = (1500, -1000)$, $H = (1000, -1000)$ and $I = (0, -1000)$ measured in meters. There are two conductive fractures in the domain $\{BG\}$ and $\{DH\}$. The fracture $\{BG\}$ has thickness $\epsilon = 5\sqrt{2}m$ and the fracture $\{DH\}$ has thickness $\epsilon = 33/\sqrt{5}m$. The permeability (hydraulic conductivity) is $\mathbb{K}_m = 10^{-8}m/s$ in the bulk and $\mathbb{K}_c = 10^{-6}m/s$ in the fractures. Dirichlet boundary condition $p = \text{height}$ is imposed on the top boundary, and homogeneous Neumann boundary condition is imposed on the rest of the boundary. Here the unknown variable p is termed as the piezometric head according to [77]. The quantity of interest is the distribution of the piezometric head p along the horizontal line at a depth of $200m$.

We apply the method (4) on a uniform triangular mesh with mesh size $h = 60$, see the left panel of Figure 3, which leads to 1,115 matrix elements and 44 fracture elements. On this mesh, the number of the globally coupled DOFs is 1,779, in which 1,691 DOFs are associated with the bulk hybrid variable \hat{p}_h , and 43 DOFs are associated with the fracture hybrid variable \hat{p}_h^c . In the right panel of Figure 3, we record the postprocessed piezometric head p_h^* in (5) along the line segment $z = -200m$, where z is the horizontal direction, along with the reference data obtained from a mimetic finite difference method on a very fine mesh (with 889,233 DOFs). We observe that the results for the proposed method on such a coarse mesh already shows a good agreement with the reference data.

4.2. Benchmark 2: Regular Fracture Network (2D). This test case is originally from [6] and is modified by [54], which simulates a regular fracture network in a square porous media. The computational domain including the fracture network and boundary conditions is shown in Figure 4. The matrix permeability is set to $\mathbb{K}_m = \mathbb{I}$, and fracture thickness is $\epsilon = 10^{-4}$. Two cases of fracture permeability was considered: (i) a highly conductive network with $\mathbb{K}_c = 10^4\mathbb{I}$, (ii) a blocking fracture with $K_b = 10^{-4}$.

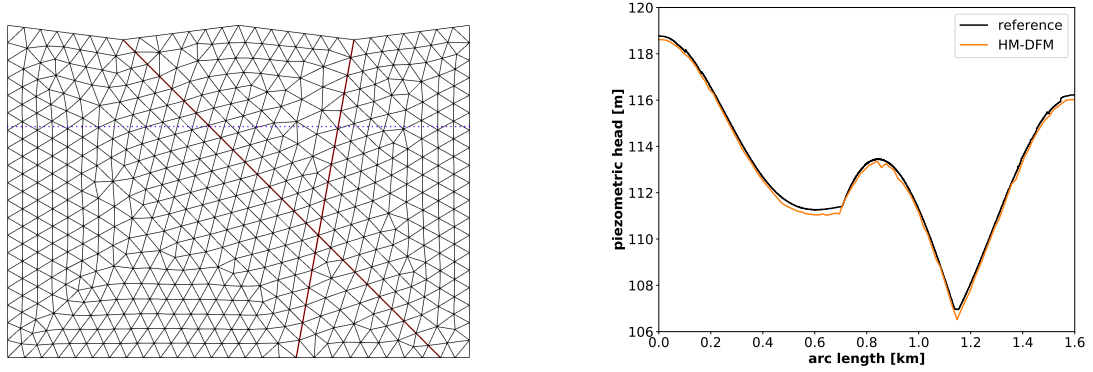


FIGURE 3. Benchmark 1. Left: computational mesh. Right: piezometric head along the line $z = -200m$ (dotted blue line on the left figure).

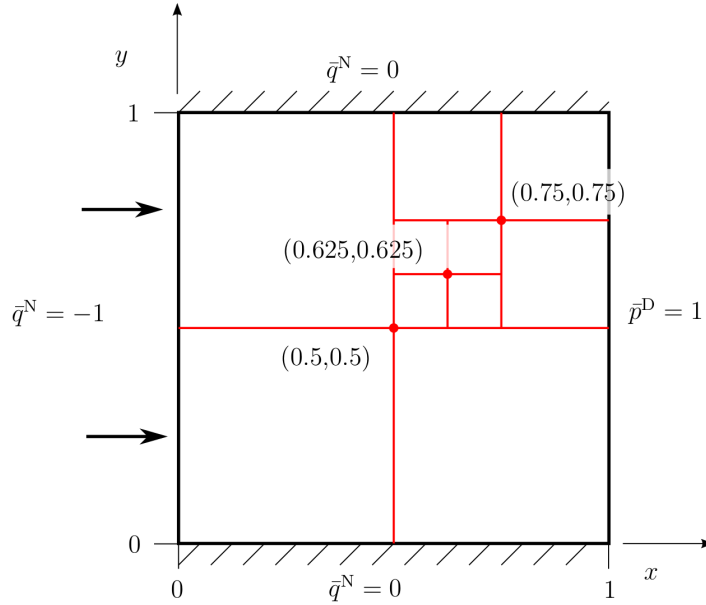


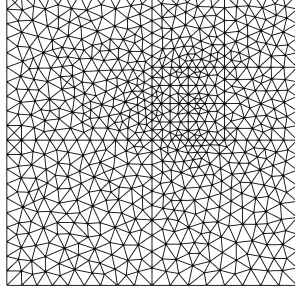
FIGURE 4. Benchmark 2. Domain and boundary conditions.

We apply the method (4) on a triangular mesh with 1,348 matrix elements and 91 fracture elements, see the left panel of Figure 5. For the blocking fracture case, we also present the result on a unfitted triangular mesh with 1,442 matrix elements.

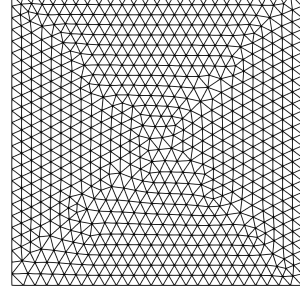
For the conductive fracture case, the number of the globally coupled DOFs is 2,127, in which 2,041 DOFs are associated with the bulk hybrid variable \hat{p}_h , and 86 DOFs are associated with the fracture hybrid variable \hat{p}_h^c . The pressure distributions along two lines, one horizontal at $y = 0.7$ and one vertical at $x = 0.5$ are shown in Figure 6, along with the reference data obtained from a mimetic finite difference method on a very fine mesh (with 1,175,056 DOFs). Similar to the previous example, we observe that the results for the proposed method show a good agreement with the reference data.

For the blocking fracture case, the number of the globally coupled DOFs is 2,041 on the fitted mesh and is 2,188 on the unfitted mesh. The pressure distribution along the lines $(0, 0.1) - (0.9, 1.0)$

is shown in Figure 7. Again, we observe a very good agreement with reference data for the results on the fitted mesh. The result on the unfitted mesh case is slightly off due to mesh nonconformity, which is expected as it could not capture the pressure discontinuity across the blocking fractures.

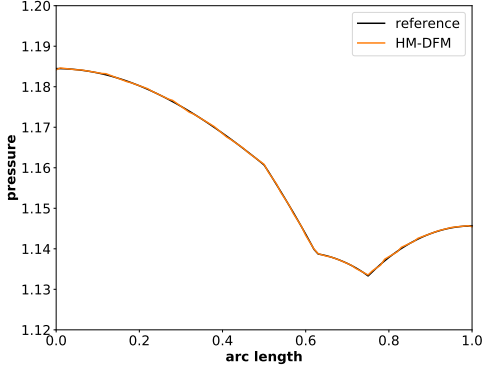


(a) a fitted mesh.

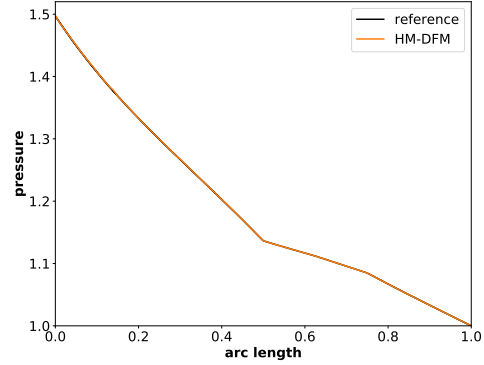


(b) a unfitted mesh.

FIGURE 5. Benchmark 2: computational meshes. The fitted mesh on the left panel is used for both conductive and blocking fracture cases. The unfitted mesh on the right panel is used only for the blocking fracture case.



(a) Horizontal line at $y = 0.7$.



(b) Vertical line at $x = 0.5$.

FIGURE 6. Benchmark 2 with conductive fractures: pressure distribution along two lines.

4.2.1. Coupling with transport and convergence study with mesh refinements. After the velocity fields are computed from the scheme (4), we feed them to the transport model (2), and solve it by using the hybrid finite volume scheme (6). We take the porosities $\phi_m = 0.1$, $\phi_c = 0.9$ in the model (2), with the initial concentrations $c_0 = c_{c,0} = 0$, and set the left boundary as the inflow boundary for the concentrations, with $c_B = c_{c,B} = 1$. The final time of simulation is $T = 0.1$. Convergence of our coupled scheme (4) and (6) is checked via a mesh refinement study, where the initial meshes are given in Figure 5, and three level of uniform mesh refinements are applied afterwards. The constant time step size is taken to be $\Delta t = 2^{-l} \times 5 \times 10^{-3}$, where l is the mesh refinement level. Since there is no analytic solution to the problem, we provide a reference solution using the coupled scheme (4) and (6) on the fourth level refined fitted mesh (with about 345k elements) with a small time step size $\Delta t = 3.125 \times 10^{-5}$. Contour of matrix concentrations of the reference solution at time $t = 0.05$ and $t = 0.1$ are presented in Figure 8, where we clearly observe the conducting and blocking effects of the respective fractures. Moreover, we plot the computed matrix concentrations

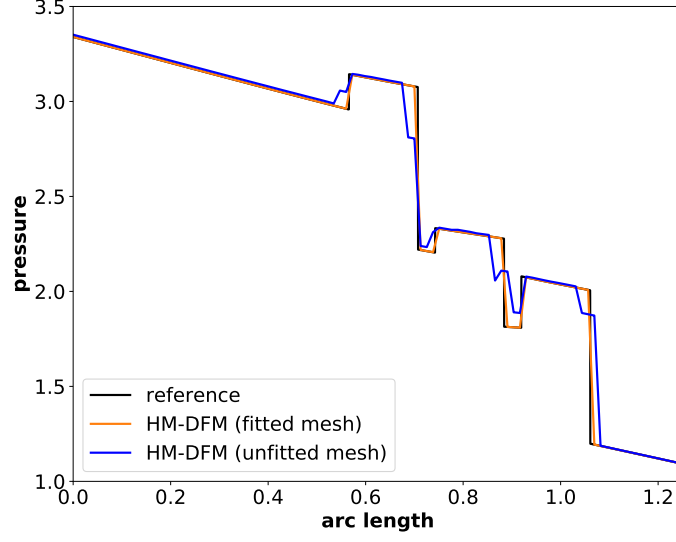


FIGURE 7. Benchmark 2 with blocking fractures: values along the line (0,0.1)–(0.9,1.0).

along the cut line $y = 0.7$ in Figure 9, where we observe convergence as the mesh refines.

Finally, the L^2 -errors in the matrix velocity and postprocessed matrix pressure, and the L^2 -errors in the matrix concentration at final time $T = 0.1$ are recorded in Table 1 for the conductive fracture case, in Table 2 for the blocking fracture case on fitted meshes and in Table 3 for the blocking fracture case on unfitted meshes. From Table 1 for the conductive fracture case, we observe that the convergence rate in the velocity approximation is first order and that in the postprocessed pressure approximation is second order, which is consistent with the expected convergence behavior of the hybrid-mixed method for the equi-dimensional case [78, 79], and the convergence rate for the concentration is about $1/2$, which is also expected for the hybridized finite volume scheme due to the concentration discontinuities in the domain. Similar convergence behavior was observed in Table 2 for the blocking fracture case on fitted meshes. From Table 3 we observe $1/2$ order convergence for all three variables, where the degraded velocity and pressure convergence is due to nonconformity of the mesh with the fractures.

mesh ref. lvl.	L^2 -err in \mathbf{u}_h	rate	L^2 -err in p_h^*	rate	L^2 -err in $c_h(T)$	rate
0	3.567e-02	–	3.786e-04	–	1.177e-01	–
1	1.954e-02	0.87	1.061e-04	1.84	8.587e-02	0.45
2	1.029e-02	0.92	7.146e-06	2.00	5.883e-02	0.55
3	4.881e-03	1.08	2.863e-05	1.89	3.541e-02	0.73

TABLE 1. Benchmark 2 with conductive fractures (fitted mesh): history of convergence for the L^2 -errors in \mathbf{u}_h , p_h^* , and $c_h(T)$ along mesh refinements. Reference solution is obtained on the fourth level refined fitted mesh with a small time step size $\Delta t = 3.125 \times 10^{-5}$.

4.3. Benchmark 3: Complex Fracture Network (2D). This test case considers a small but complex fracture network that includes permeable and blocking fractures. The domain and boundary conditions are shown in Figure 10. The exact coordinates for the fracture positions are provided

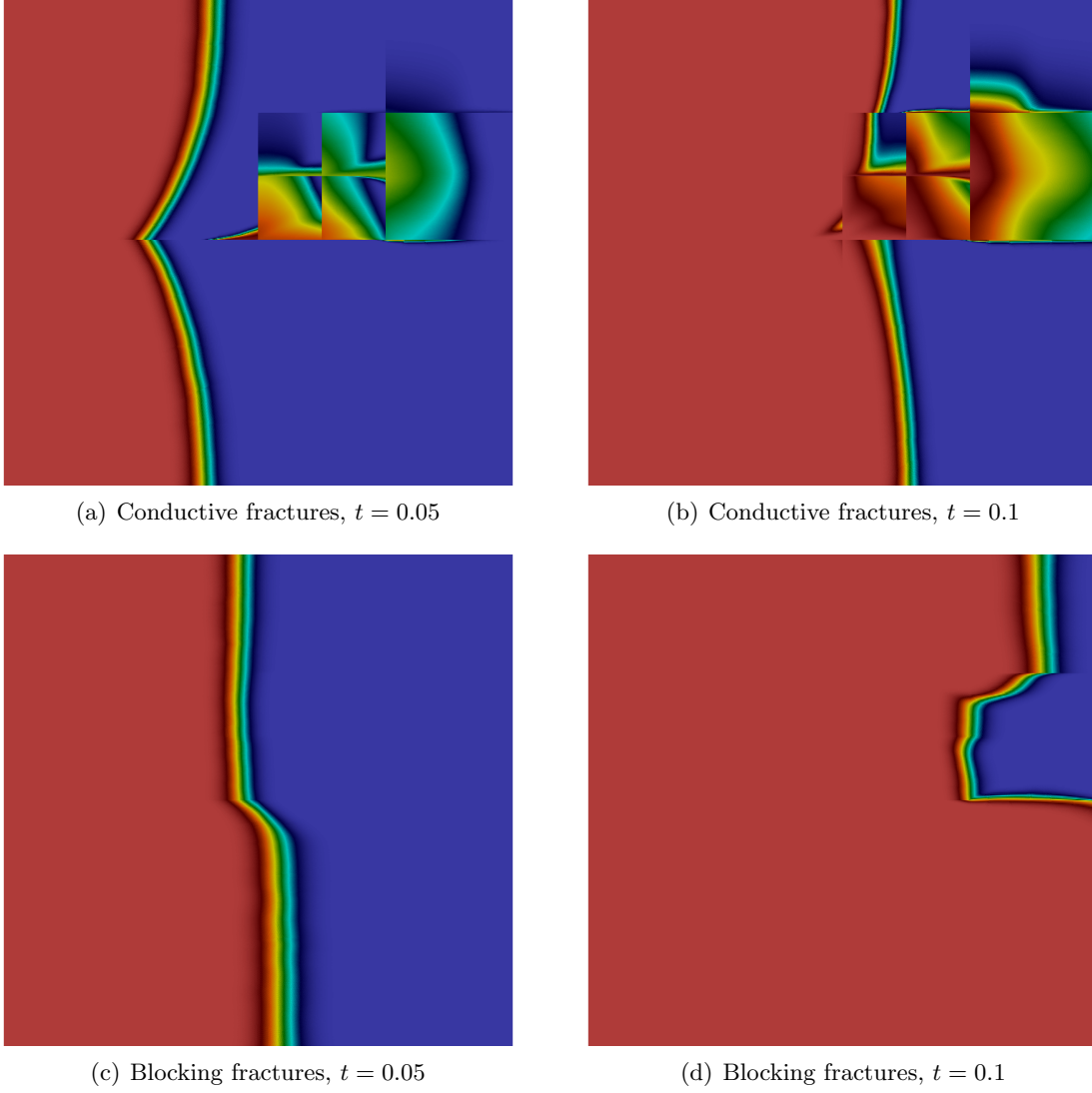
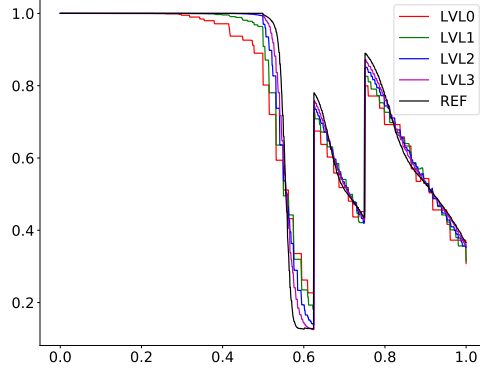


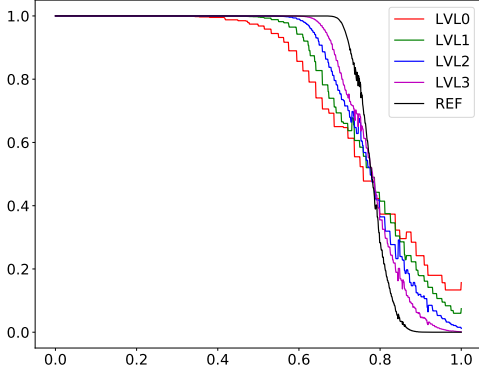
FIGURE 8. Benchmark 2: Matrix concentration at time $t = 0.05$ (left) and $t = 0.1$ (right). Top row: conductive fractures. Bottom row: blocking fractures. Color range: 0(blue)–1(red). Solution obtained on the fourth level refined mesh with a small time step size $\Delta t = 3.125 \times 10^{-5}$.

mesh ref. lvl.	L^2 -err in \mathbf{u}_h	rate	L^2 -err in p_h^*	rate	L^2 -err in $c_h(T)$	rate
0	1.358e-02	–	2.406e-04	–	1.396e-01	–
1	7.098e-03	0.94	6.402e-05	1.91	1.025e-01	0.44
2	3.607e-03	0.98	1.630e-05	1.97	7.149e-02	0.52
3	1.666e-03	1.11	3.566e-06	2.19	4.572e-02	0.64

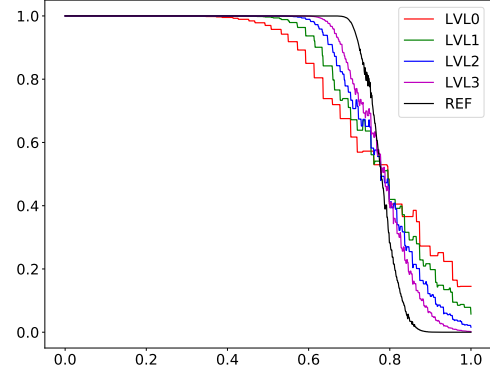
TABLE 2. Benchmark 2 with blocking fractures (fitted mesh): history of convergence for the L^2 -errors in \mathbf{u}_h , p_h^* , and $c_h(T)$ along mesh refinements. Reference solution is obtained on the fourth level refined fitted mesh with a small time step size $\Delta t = 3.125 \times 10^{-5}$.



(a) Conductive fractures, fitted mesh



(b) Blocking fractures, fitted mesh



(c) Blocking fractures, unfitted mesh

FIGURE 9. Benchmark 2: Matrix concentration along the line $y = 0.7$ at time $t = 0.1$ for the solution on different meshes. LVL stands for the number of mesh refinement levels. Reference solution is obtained on the fourth level refined fitted mesh with a small time step size $\Delta t = 3.125 \times 10^{-5}$.

mesh ref. lvl.	L^2 -err in \mathbf{u}_h	rate	L^2 -err in p_h^*	rate	L^2 -err in $c_h(T)$	rate
0	7.611e-02	—	8.295e-02	—	1.424e-01	—
1	5.357e-02	0.51	5.890e-02	0.49	1.050e-01	0.44
2	3.991e-02	0.42	4.088e-02	0.53	7.418e-02	0.50
3	2.634e-02	0.60	2.899e-02	0.50	4.882e-02	0.60

TABLE 3. Benchmark 2 with blocking fractures (unfitted mesh): history of convergence for the L^2 -errors in \mathbf{u}_h , p_h^* , and $c_h(T)$ along mesh refinements. Reference solution is obtained on the fourth level refined fitted mesh with a small time step size $\Delta t = 3.125 \times 10^{-5}$.

in [54, Appendix C]. The fracture network contains ten straight immersed fractures. The fracture thickness is $\epsilon = 10^{-4}$ for all fractures, and permeability is $\mathbb{K}_c = 10^4$ for all fractures except for

fractures 4 and 5 which are blocking fractures with $K_b = 10^{-4}$. Note that we are considering two subcases a) and b) with a pressure gradient which is predominantly vertical and horizontal respectively.

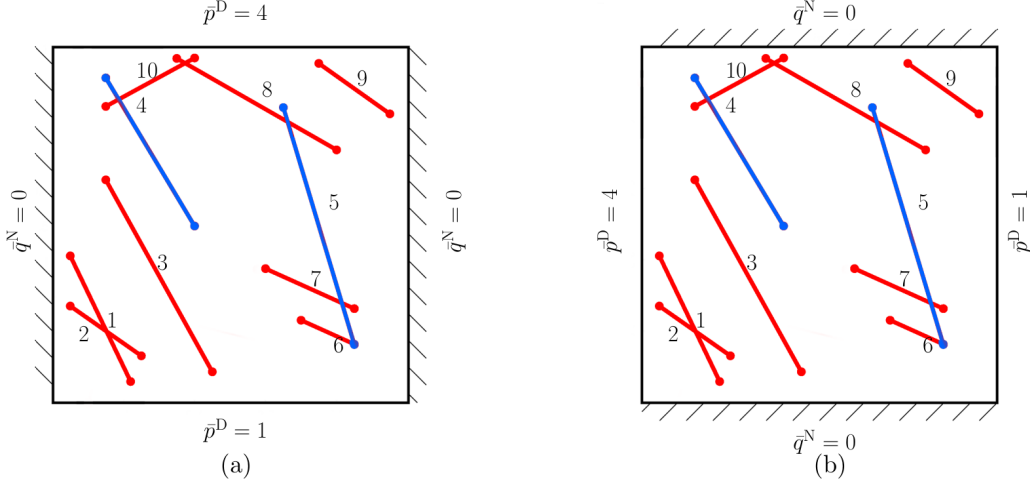


FIGURE 10. Benchmark 3: computational domain and boundary conditions.

We apply the method (4) on two set of meshes: a triangular fitted mesh with 1,332 matrix elements and 88 fracture elements which was provided in the git repository <https://git.iws.uni-stuttgart.de/benchmarks/fracture-flow>, see left of Figure 11, and a triangular immersed fitted mesh with 1,370 matrix elements and 211 fracture elements obtained from a background unfitted mesh using the immersing mesh technique introduced in Section 3.6, see right of Figure 11. The globally coupled DOFs is 2,066 for the fitted mesh, and is 2,211 for the immersed mesh.

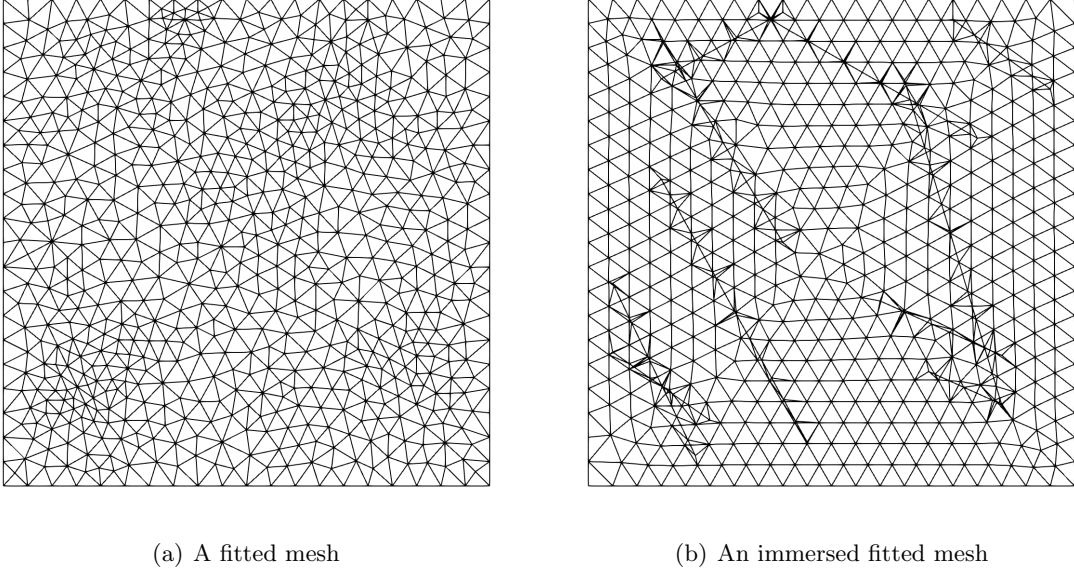


FIGURE 11. Benchmark 3: computational meshes.

The pressure distributions along the lines $(0, 0.5) - (1.0, 0.9)$ are shown in Figure 12. We observe

that the results on the two meshes are very close to each other, and they are in good agreements with the reference data obtained from a mimetic finite difference method on a very fine mesh with 1.8 million DOFs.

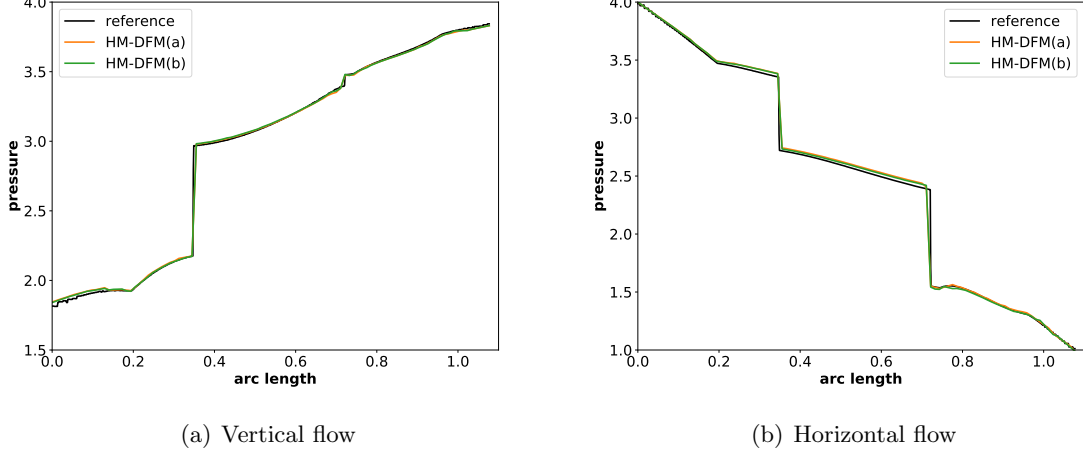


FIGURE 12. Benchmark 3: pressure distribution along line $(0, 0.5) - (1, 0.9)$. HDG-DFM(a) is the numerical solution on the fitted mesh in Figure 11 (a), HDG-DFM(b) is the numerical solution on the immersed fitted mesh in Figure 11 (b).

4.4. Benchmark 4: a Realistic Case (2D). We consider a real set of fractures from an interpreted outcrop in the Sotra island, near Bergen in Norway. The size of the domain is $700\text{ m} \times 600\text{ m}$ with uniform scalar permeability $\mathbb{K}_m = 10^{-14}\text{m}^2$. The set of fractures is composed of 64 line segments, in which the permeability is $\mathbb{K}_c = 10^{-8}\text{m}^2$. The fracture thickness is $\epsilon = 10^{-2}\text{m}$. The exact coordinates for the fracture positions are provided in the above mentioned git repository. The domain along with boundary conditions is given in Figure 13. Similar to the previous example, we apply the method (4) on two set of conforming meshes: a fitted mesh consists of 10,807 matrix elements and 1,047 fracture elements provided in <https://git.iws.uni-stuttgart.de/benchmarks/fracture-flow>, see left of Figure 14, and an immersed fitted mesh consists of 5,473 matrix elements and 1541 fracture elements obtained from a background unfitted mesh using the immersing mesh technique introduced in Section 3.6, see right of Figure 14. The number of the globally coupled DOFs is 17,253 for the fitted mesh (a), and 9,753 for the immersed mesh (b).

The pressure distribution along the two lines $y = 500\text{m}$ and $x = 625\text{m}$ are shown in Figure 15, along with the results for the mortar-DFM method with 25,258 DOFs from [54]. We observe that the three results are in good agreements with each other, with the HDG-DFM(b) using the least amount of DOFs.

4.5. Benchmark 5: Single Fracture (3D). This is the first benchmark case proposed in [69]. To be consistent with the notation in [69], the pressure and permeabilities are renamed as hydraulic head and hydraulic conductivities, respectively for this test case and the three examples following. Figure 16 illustrates the geometrical description. Here the domain Ω is a cube-shaped region $(0\text{m}, 100\text{m}) \times (0\text{m}, 100\text{m}) \times (0\text{m}, 100\text{m})$ which is crossed by a conductive planar fracture, Ω_2 , with a thickness of $\epsilon = 10^{-2}\text{m}$. The matrix domain consists of subdomains $\Omega_{3,1}$, above the fracture, and $\Omega_{3,2}$ and $\Omega_{3,3}$ below. The subdomain $\Omega_{3,3}$ represents a heterogeneity within the rock matrix. The matrix conductivities are given in Figure 16, and the fracture conductivity is $\mathbb{K}_c = 0.1$ so that

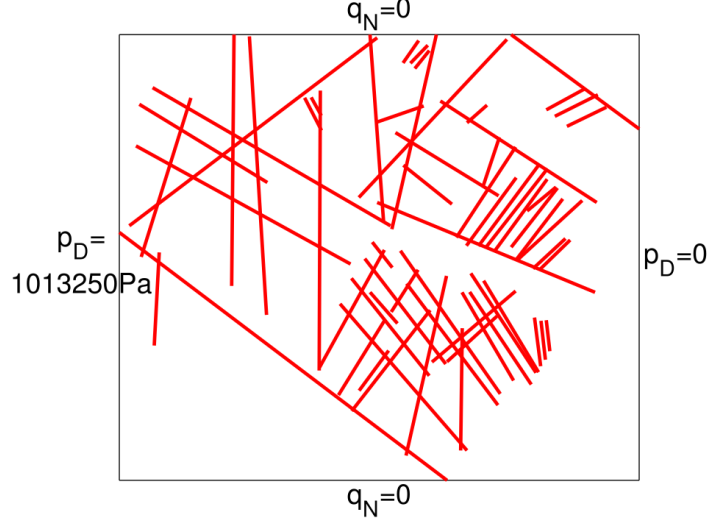
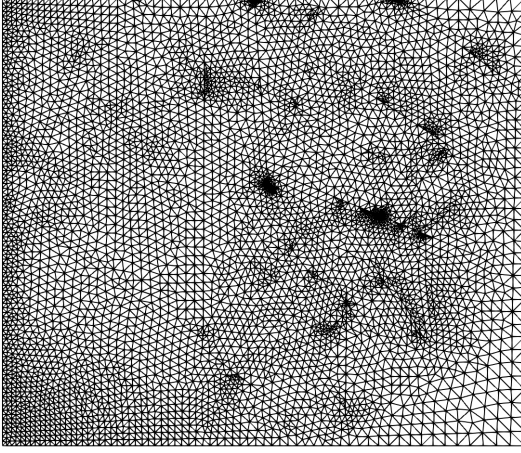
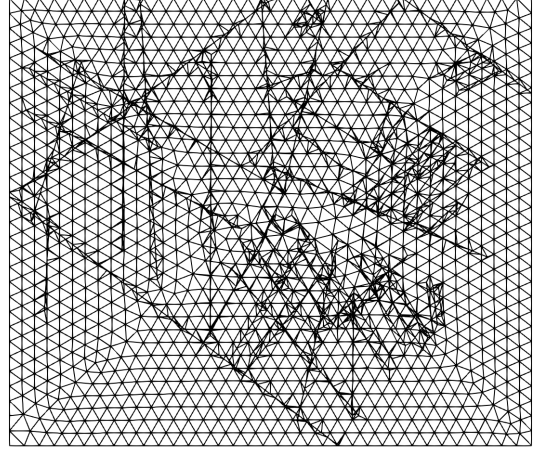


FIGURE 13. Benchmark 4: Computational domain and boundary conditions.



(a) A fitted mesh



(b) An immersed fitted mesh

FIGURE 14. Benchmark 4: computational meshes.

$\epsilon \mathbb{K}_c = 10^{-3}$. Inflow into the system occurs through a narrow band defined by $\{0m\} \times (0m, 100m) \times (90m, 100m)$. Similarly, the outlet is a narrow band defined by $(0m, 100m) \times \{0m\} \times (0m, 10m)$. At the inlet and outlet bands, we impose the hydraulic head $h_{in} = 4m$ and $h_{out} = 1m$ respectively. The remaining parts of the boundary are assigned no-flow conditions. Following the setup in [69], we set $c_B = 0.01m^{-3}$ at the inlet boundary for the transport problem. The matrix porosity ϕ is taken to be 0.2 on $\Omega_{3,1} \cup \Omega_{3,2}$ and 0.25 on $\Omega_{3,3}$, and the fracture porosity ϕ_c is taken to be 0.4. The final time of simulation is $T = 10^9 s$, and the time step size is $\Delta t = 10^7 s$.

We perform the method (4) and (6) on a coarse tetrahedral mesh with 10,232 matrix elements and 448 fracture elements and a fine tetrahedral mesh with 111,795 matrix elements and 1,758 fracture

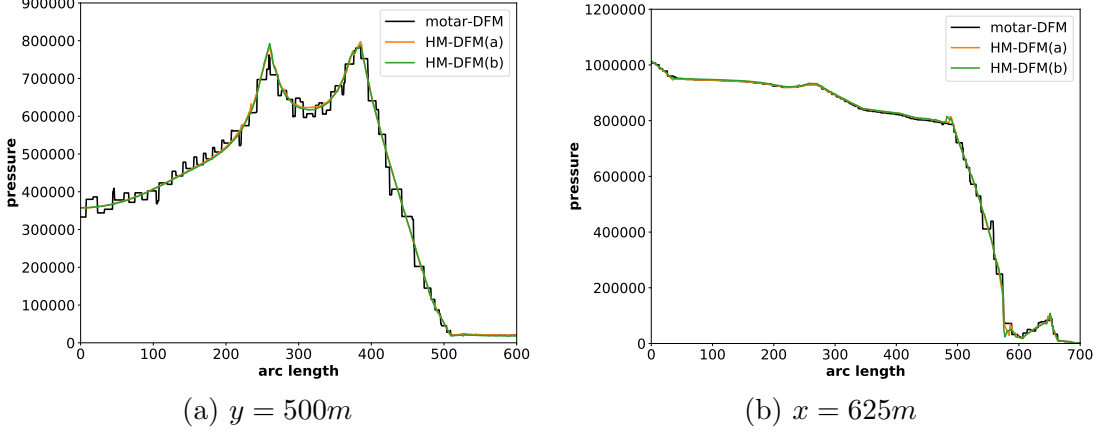


FIGURE 15. Benchmark 4: Pressure distribution along lines $y = 500m$ (left) and $x = 625m$ (right). HDG-DFM(a) is the numerical solution on the fitted mesh in Figure 14(a), HDG-DFM(b) is the numerical solution on the immersed fitted mesh in Figure 14(b).

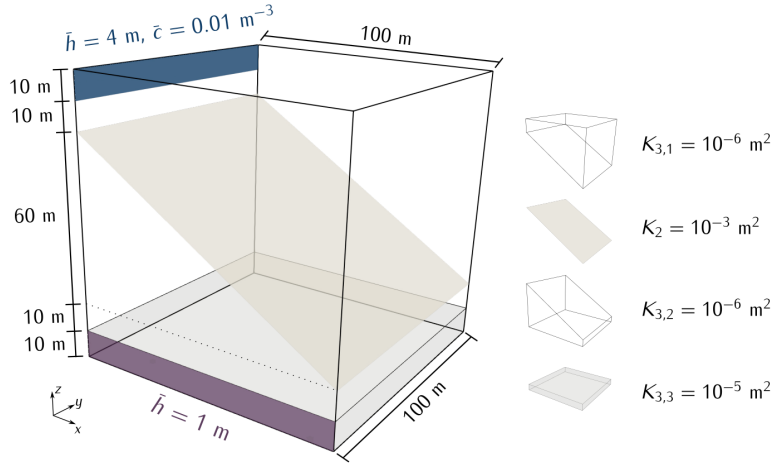


FIGURE 16. Benchmark 5: Conceptual model and geometrical description of the domain.

elements. The number of the globally coupled DOFs on the coarse mesh is 23,377, while that on the fine mesh is 235,619. The hydraulic head along the line $(0m, 100m, 100m) - (100m, 0m, 0m)$ is shown in Figure 17, along with reference data and published spread provided in the git repository <https://git.iws.uni-stuttgart.de/benchmarks/fracture-flow-3d>. The reference data in Figure 17 is obtained from the USTUTT-MPFA method on a mesh with approximately 1 million matrix elements, while the shaded region depicts the area between the 10th and the 90th percentile of the published results in [69] on mesh refinement level 1 (left, $\sim 10k$ cells) and refinement level 2 (right, $\sim 100k$ cells). The match number results from evaluating at 100 evenly distributed evaluation points if the value for the HM-DFM method is between the respective lower and upper value. We observe that our result agrees with the reference values quite well, especially on the fine mesh.

Moreover, we plot the matrix concentration along the line $(0m, 100m, 100m) - (100m, 0m, 0m)$ in Figure 18, and the fracture concentration along the line $(0m, 100m, 80m) - (100m, 0m, 20m)$ at final time $T = 10^9 s$ in Figure 19, together with the published spread provided in the git repository, which depicts the area between the 10th and the 90th percentile of the published results in [69]

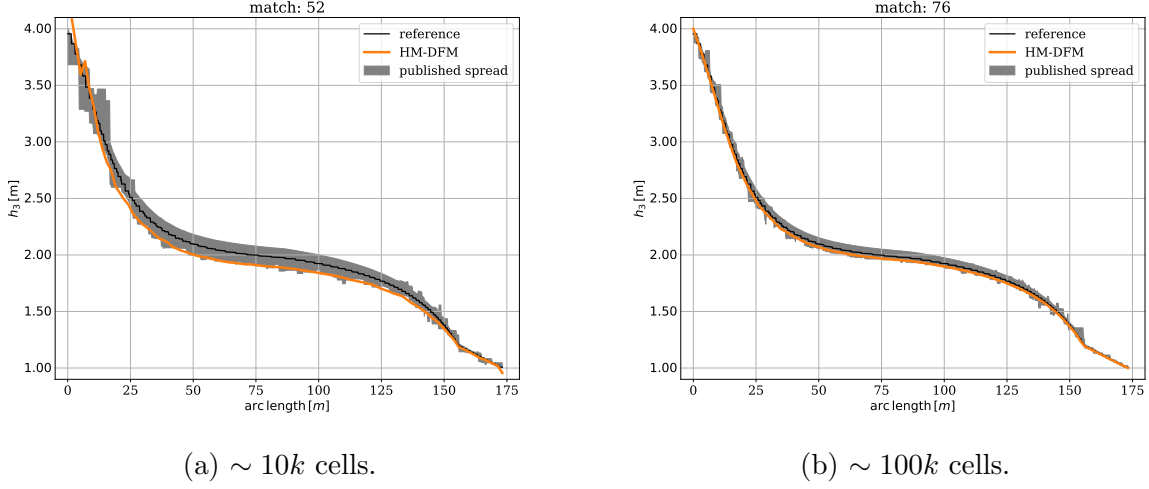


FIGURE 17. Benchmark 5: Hydraulic head in the matrix over the line (0m, 100m, 100m)–(100m, 0m, 0m). Left: results on a coarse mesh with about 10k cells. Right: results on a fine mesh with about 100k cells.

using similar first order finite volume schemes with implicit Euler time stepping and $\Delta t = 10^7 s$. We observe that our results agree quite well with the provided data.

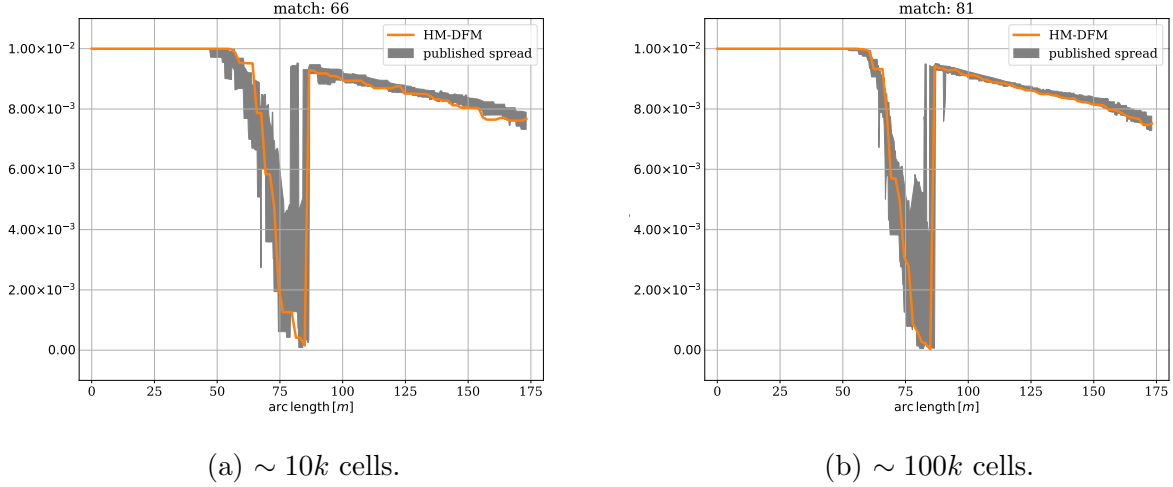


FIGURE 18. Benchmark 5: Hydraulic head in the matrix over the line (0m, 100m, 100m)–(100m, 0m, 0m). Left: results on a coarse mesh with about 10k cells. Right: results on a fine mesh with about 100k cells.

4.6. Benchmark 6: Regular Fracture Network (3D). This is the second benchmark case proposed in [69], which is a 3D analog of Benchmark 2. The domain is given by the unit cube $\Omega = (0m, 1m)^3$ and contains 9 regularly oriented fractures, as illustrated in Figure 20. Dirichlet boundary condition $p = \bar{h} = 1m$ is imposed on the boundary $\Gamma_D = \{(x, y, z) \in \partial\Omega : x, y, z > 0.875m\}$, Neumann boundary condition $\mathbf{u} \cdot \mathbf{n} = -1m/s$ is imposed on the boundary $\partial\Omega_{in} = \{(x, y, z) \in \partial\Omega : x, y, z < 0.25m\}$, and no-flow boundary condition is imposed on the remaining boundaries. The heterogeneous matrix conductivity is illustrated in Figure 20, and the fracture conductivity is either

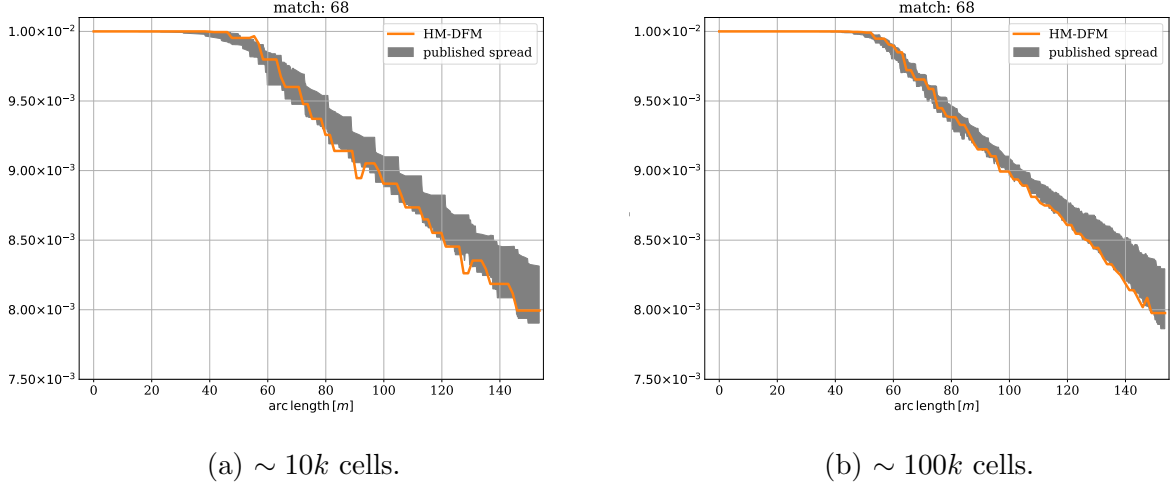


FIGURE 19. Benchmark 5: Fracture concentration over the line (0m, 100m, 80m)–(100m, 0m, 20m). Left: results on a coarse mesh with about 10k cells. Right: results on a fine mesh with about 100k cells.

$\mathbb{K}_c = 10^4 \text{m}^2$, which represents a conductive fracture or $K_b = 10^{-4} \text{m}^2$ which represents a blocking fracture. The fracture thickness is $\epsilon = 10^{-4} \text{m}$. For the transport equation, matrix porosity is taken to be $\phi = 0.1$, conductive fracture concentration is $\phi_c = 0.9$, and the inflow boundary condition $c_B = 1 \text{m}^{-3}$ is set on the inlet boundary $\partial\Omega_{in}$. Final time of the simulation is $T = 0.25 \text{s}$.

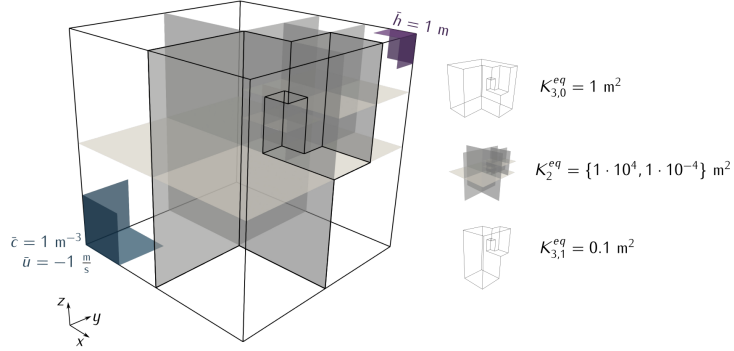


FIGURE 20. Benchmark 6: Conceptual model and geometrical description of the domain.

We perform the method (4) on a coarse *fitted* tetrahedral mesh with 4,375 matrix elements and 944 fracture elements and a fine tetrahedral mesh with 36,336 matrix elements and 4,524 fracture elements. The number of the globally coupled DOFs on the coarse mesh is 13,373 for the conductive fracture case and 8,334 for the blocking fracture case (only DOFs for \hat{p}_h are global DOFs in this case), while that on the fine mesh is 94,738 for the conductive fracture case and 70,881 for the blocking fracture case. The hydraulic head along the diagonal line (0m, 0m, 0m)–(1m, 1m, 1m) is shown in Figure 21 for the conductive fracture case and in Figure 22 for the blocking fracture case. We observe that our results agree with the reference values very well, which were obtained from the USTUTT-MPFA method on a mesh with approximately 1 million matrix elements. The small derivation of our result on the left panel of Figure 21 with the reference data is acceptable due to the use of a very coarse mesh.

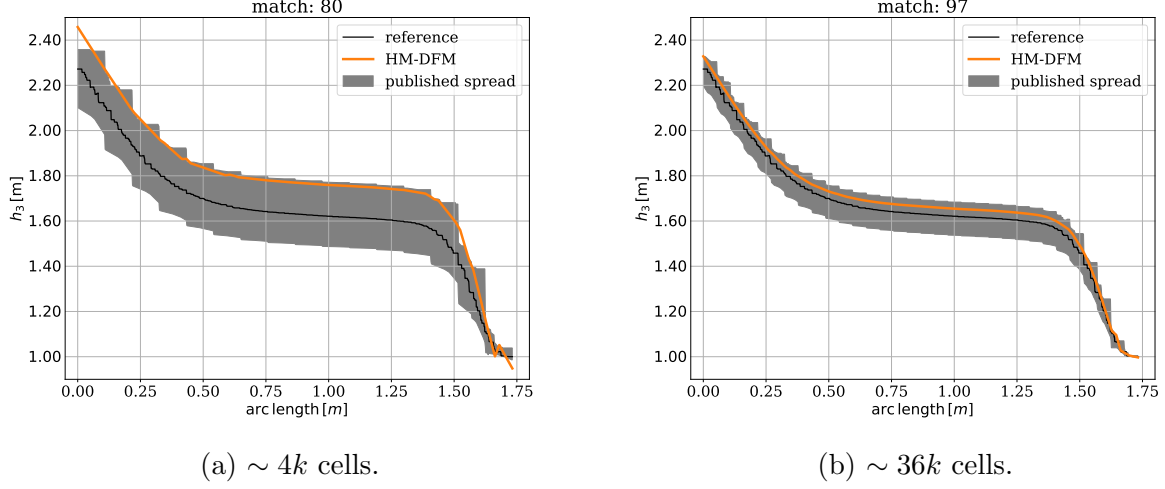


FIGURE 21. Benchmark 6 (conductive fractures): Hydraulic head in the matrix over the line $(0m, 0m, 0m) - (1m, 1m, 1m)$. Left: results on a coarse mesh with about $4k$ cells. Right: results on a fine mesh with about $36k$ cells.

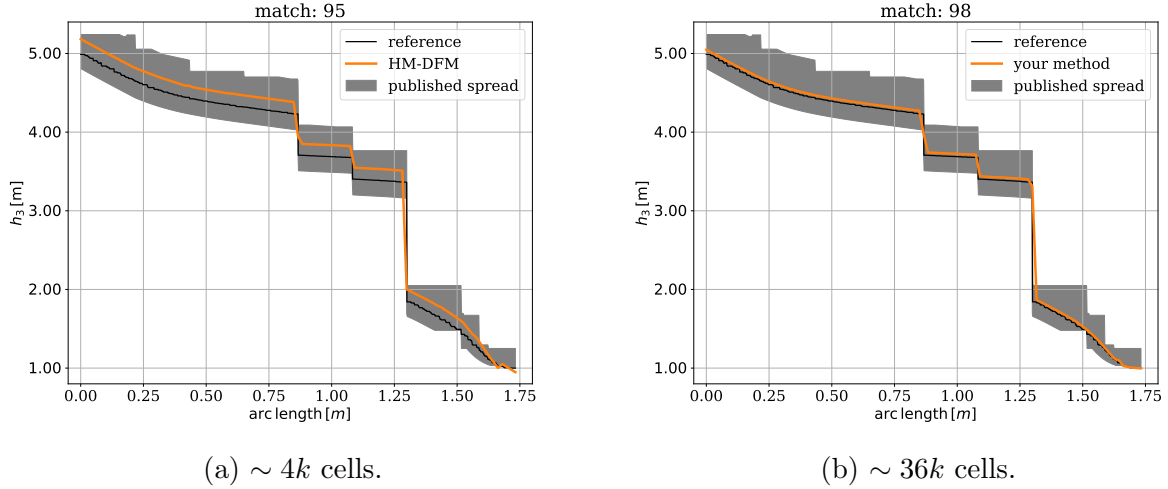


FIGURE 22. Benchmark 6 (blocking fractures): Hydraulic head in the matrix over the line $(0m, 0m, 0m) - (1m, 1m, 1m)$. Left: results on a coarse mesh with about $4k$ cells. Right: results on a fine mesh with about $36k$ cells.

We further performed a convergence study of the flow and transport solvers (4) and (6) via mesh refinements, and record the L^2 -errors in matrix velocity and postprocessed pressure, and the L^2 -errors in matrix concentration at final time $t = 0.25$ in Table 4 for the conductive fracture case and in Table 5 for the blocking fracture case, where the initial mesh is the coarse one with 4,375 tetrahedral elements. A total of three uniform mesh refinements was performed, and the solution on the third level mesh was used as the reference solution to calculate the associated errors. The time step size is taken to be $\Delta t = 2^{-l} \times 2.5 \times 10^{-3}s$, where l is the mesh refinement level. On the finest mesh, there are about 2.25 million tetrahedral elements and 4.5 million globally coupled DOFs. From both tables, we observe convergence of our schemes, and in particular the convergence

rate for the velocity is approaching first order, that for the postprocessed pressure is approaching second order, and for the concentration is about first order.

mesh ref. lvl.	L^2 -err in \mathbf{u}_h	rate	L^2 -err in p_h^*	rate	L^2 -err in $c_h(T)$	rate
0	1.789e-01	—	1.456e-01	—	1.496e-01	—
1	1.120e-01	0.68	5.886e-02	1.31	9.645e-02	0.63
2	6.181e-02	0.86	1.852e-02	1.67	5.102e-02	0.92

TABLE 4. Benchmark 6 with conductive fractures (fitted mesh): history of convergence for the L^2 -errors in \mathbf{u}_h , p_h^* , and $c_h(T)$ along mesh refinements. Reference solution is obtained on the third level refined fitted mesh with about 2.25 million matrix elements and time step size $\Delta t = 3.125 \times 10^{-4}$.

mesh ref. lvl.	L^2 -err in \mathbf{u}_h	rate	L^2 -err in p_h^*	rate	L^2 -err in $c_h(T)$	rate
0	1.791e-01	—	1.533e-01	—	1.288e-01	—
1	1.118e-01	0.68	6.080e-02	1.33	8.139e-02	0.66
2	6.172e-02	0.86	1.891e-02	1.68	3.939e-02	1.05

TABLE 5. Benchmark 6 with blocking fractures (fitted mesh): history of convergence for the L^2 -errors in \mathbf{u}_h , p_h^* , and $c_h(T)$ along mesh refinements. Reference solution is obtained on the third level refined fitted mesh with about 2.25 million matrix elements and time step size $\Delta t = 3.125 \times 10^{-4}$.

Finally, in Figure 23 we plot slices of concentrations computed on the 3rd refined mesh at final time $t = 0.25$ along the five vertical planes $x = 0.1, x = 0.3, x = 0.5, x = 0.7$ and $x = 0.9$, and in Figure 24 we plot the evolution of mean concentration over time on the following three regions:

$$\begin{aligned}\Omega_A &:= (0.5m, 1m) \times (0m, 0.5m) \times (0m, 0.5m), \\ \Omega_B &:= (0.5m, 0.75m) \times (0.5m, 0.75m) \times (0.75m, 1m), \\ \Omega_C &:= (0.75m, 1m) \times (0.75m, 1m) \times (0.5m, 0.75m).\end{aligned}$$

$$\begin{aligned}\Omega_A &:= (0.5m, 1m) \times (0m, 0.5m) \times (0m, 0.5m), \\ \Omega_B &:= (0.5m, 0.75m) \times (0.5m, 0.75m) \times (0.75m, 1m), \\ \Omega_C &:= (0.75m, 1m) \times (0.75m, 1m) \times (0.5m, 0.75m).\end{aligned}$$

From the results in Figure 23, we clearly observe the different flow pattern for the conductive fracture case in the first row and the blocking fracture case in the second row. We further note that the mean concentrations reported in Figure 24 were presented in [69, Figure 10] (only) on the coarse mesh with about $4k$ matrix elements and a coarse time step size $\Delta t = 2.5 \times 10^{-3}s$. Our results on four set of meshes are close to each other and improve slightly as the mesh and time step size refines, and they are also qualitatively similar to the majority of the coarse-grid results in [69, Figure 10].

4.7. Benchmark 7: Network with Small Features (3D). This is the third benchmark case proposed in [69], in which small geometric features exist that may cause trouble for conforming meshing strategies. The domain is the box $\Omega = (0m, 1m) \times (0m, 2.25m) \times (0m, 1m)$, containing 8 fractures; see Figure 25. Homogeneous Dirichlet boundary condition is imposed on the outlet boundary

$$\partial\Omega_{out} := \{(x, y, z) : 0 < x < 1, y = 2.25, z < 1/3 \text{ or } z > 2/3\},$$

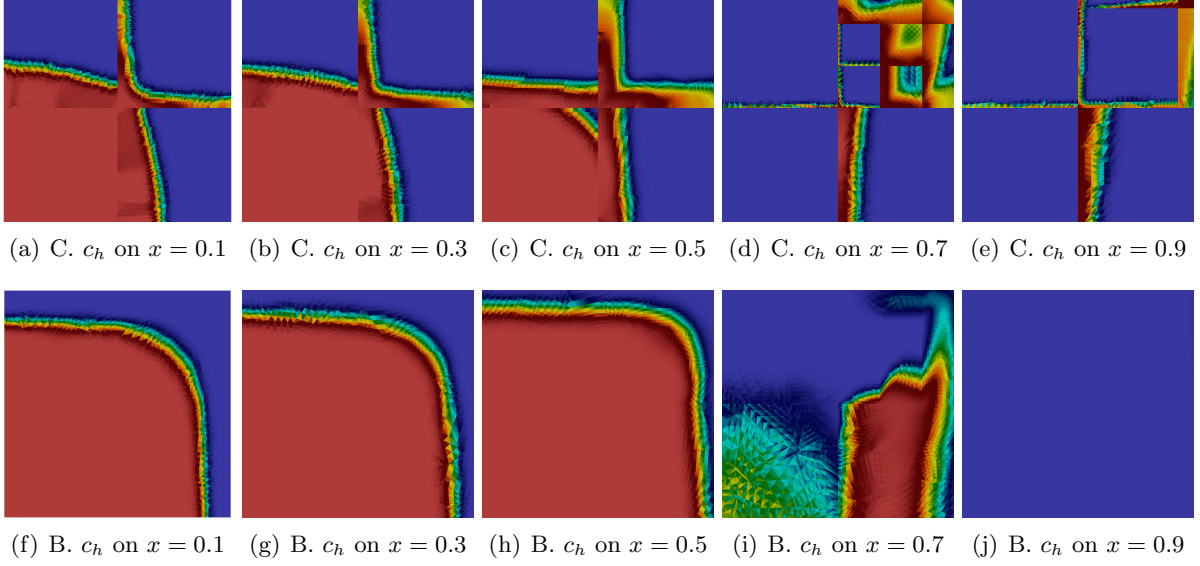


FIGURE 23. Benchmark 6: Matrix concentration at time $t = 0.25$ along the five vertical planes $x = 0.1, x = 0.3, x = 0.5, x = 0.7$ and $x = 0.9$. Top row: conductive fractures. Bottom row: blocking fractures. Color range: 0 (blue)– 1 (red).

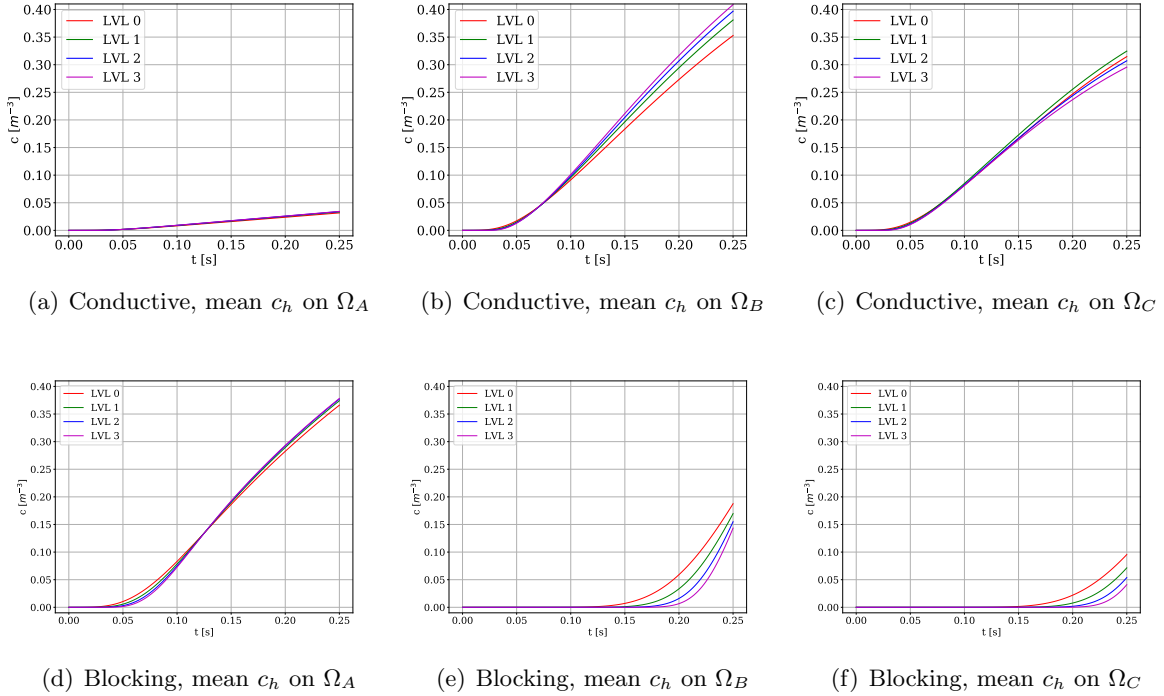


FIGURE 24. Benchmark 6: Mean matrix concentration over time on Ω_A (left), Ω_B (middle), and Ω_C (right). Top row: conductive fractures. Bottom row: blocking fractures. LVL stands for the number of mesh refinement levels.

inflow boundary condition $\mathbf{u} \cdot \mathbf{n} = -1\text{m/s}$ is imposed on the inlet boundary

$$\partial\Omega_{in} := \{(x, y, z) : 0 < x < 1, y = 0, 1/3 < z < 2/3\},$$

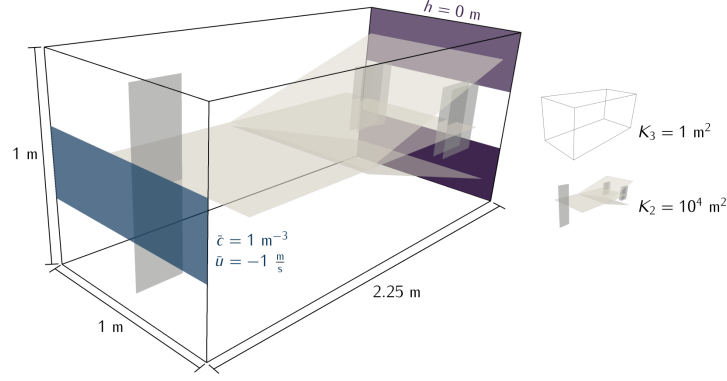


FIGURE 25. Benchmark 7: Conceptual model and geometrical description of the domain.

and no-flow boundary condition is imposed on the remaining boundaries. The conductivity in the matrix is $\mathbb{K}_m = 1 \text{ m}^2$, and that in the fracture is $\mathbb{K}_c = 10^4 \text{ m}^2$. Fracture thickness is $\epsilon = 0.01 \text{ m}$.

We perform the method (4) on a coarse tetrahedral mesh with 31,812 matrix elements and 3,961 fracture elements and a fine tetrahedral mesh with 147,702 matrix elements and 9,441 fracture elements. The number of the globally coupled DOFs on the coarse mesh is 83,022, while that on the fine mesh is 343,359. The hydraulic head along the line $(0.5 \text{ m}, 1.1 \text{ m}, 0 \text{ m}) - (0.5 \text{ m}, 1.1 \text{ m}, 1 \text{ m})$ is shown in Figure 26, where the reference data is obtained with the USTUTT-MPFA scheme on a grid with approximately 10^6 matrix cells. Here we observe a very good agreement with the reference data even on the coarse mesh.

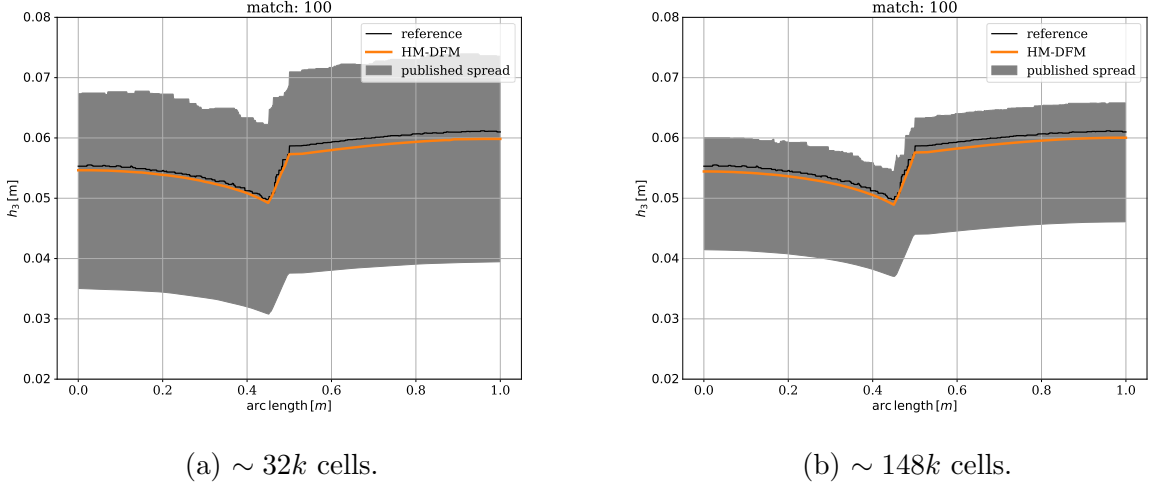


FIGURE 26. Benchmark 7: Hydraulic head in the matrix over the line $(0.5 \text{ m}, 1.1 \text{ m}, 0 \text{ m}) - (0.5 \text{ m}, 1.1 \text{ m}, 1 \text{ m})$. Left: results on a coarse mesh with about $32k$ cells. Right: results on a fine mesh with about $148k$ cells.

4.8. Benchmark 8: Field Case (3D). This is the last benchmark case proposed in [69]. The geometry is based on a postprocessed outcrop from the island of Algerøyna, outside Bergen, Norway, which contains 52 fracture. The simulation domain is the box $\Omega = (-500 \text{ m}, 350 \text{ m}) \times (100 \text{ m}, 1500 \text{ m}) \times (-100 \text{ m}, 500 \text{ m})$. The fracture geometry is depicted in Figure 27. Homogeneous

Dirichlet boundary condition is imposed on the outlet boundary

$$\partial\Omega_{out} := \underbrace{\{-500\} \times (100, 400) \times (-100, 100)}_{\partial\Omega_{out,0}} \cup \underbrace{\{350\} \times (100, 400) \times (-100, 100)}_{\partial\Omega_{out,1}}$$

uniform unit inflow $\mathbf{u} \cdot \mathbf{n} = 1\text{m/s}$ is imposed on the inlet boundary

$$\partial\Omega_{in} := \underbrace{\{-500\} \times (1200, 1500) \times (300, 500)}_{\partial\Omega_{in,0}} \cup \underbrace{(-500, -200) \times \{1500\} \times (300, 500)}_{\partial\Omega_{in,1}}.$$

Conductivity is $\mathbb{K}_m = 1\text{m}^2$ in the matrix, and $\mathbb{K}_c = 10^4\text{m}^2$ in the fracture. Fracture thickness is $\epsilon = 10^{-2}\text{m}$.

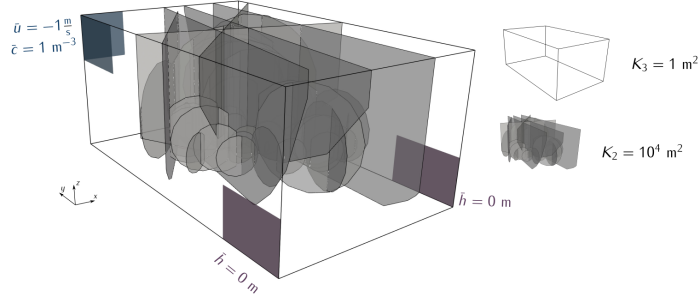


FIGURE 27. Benchmark 8: Conceptual model and geometrical description of the domain.

We perform the method (4) on a tetrahedral mesh with 241,338 matrix elements and 47,154 fracture elements. The number of the globally coupled DOFs is 696,487.

The hydraulic head along the two diagonal lines $(-500\text{m}, 100\text{m}, -100\text{m})-(350\text{m}, 1500\text{m}, 500\text{m})$ and $(350\text{m}, 100\text{m}, -100\text{m})-(-500\text{m}, 1500\text{m}, 500\text{m})$ are shown in Figure 28, along with published results from [69]. Similar to Benchmark 4 in 2D, no reference data on refined meshes was provided for this problem due to its complexity. Comparing with the published results in Figure 28 we observe that our method still performs quite well.

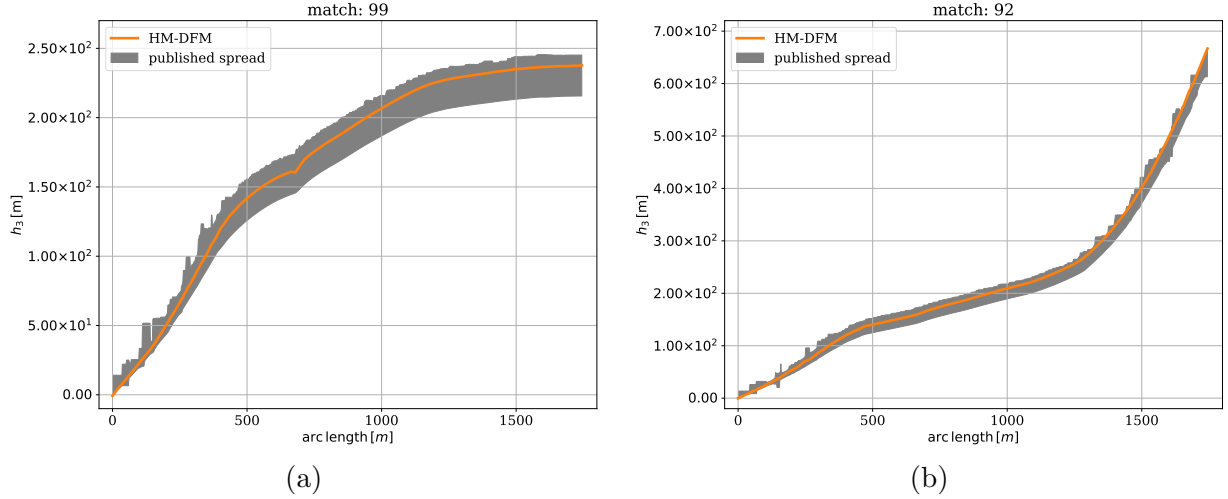


FIGURE 28. Benchmark 8: Hydraulic head across the domain. (a): Profile from outlet $\partial\Omega_{out,0}$ towards the opposite corner. (b): Profile from outlet $\partial\Omega_{out,1}$ towards the opposite corner $\partial\Omega_{in}$.

5. CONCLUSION

A novel hybrid-mixed method for single-phase flow in fractured porous media has been presented. Distinctive features of the scheme includes local mass conservation, symmetric positive definite linear system, and allowing the computational mesh to be completely non-conforming to the blocking fractures.

Ample benchmark tests show the excellent performance of the proposed scheme, which is also highly competitive with existing work in the literature. Extension to the method to more complex fractured flow models and adaptation of the method to more general meshes consists of our on-going work. We will also investigate efficient preconditioning procedures for the associated linear system problem in the near future.

REFERENCES

- [1] S. Matthäi, H. Nick, C. Pain, and I. Neuweiler, “Simulation of Solute Transport Through Fractured Rock: A Higher-Order Accurate Finite-Element Finite-Volume Method Permitting Large Time Steps,” *Transport in Porous Media*, vol. 83, pp. 289–318, 2010.
- [2] M. Vasilyeva, M. Babaei, E. Chung, and D. Spiridonov, “Multiscale modeling of heat and mass transfer in fractured media for enhanced geothermal systems applications,” *Appl. Math. Model.*, vol. 67, pp. 159–178, 2019.
- [3] M. Golian, H. Katibeh, V. P. Singh, K. Ostad-Ali-Askari, and H. Rostami, “Prediction of tunnelling impact on flow rates of adjacent extraction water wells,” *Quarterly Journal of Engineering Geology and Hydrogeology*, vol. 53, no. 2, pp. 236–251, 2020.
- [4] G. I. Barenblatt, I. P. Zheltov, and I. N. Kochina, “Basic concepts in the theory of seepage of homogeneous liquids in fissured rocks [strata],” *Journal of applied mathematics and mechanics*, vol. 24, no. 5, pp. 1286–1303, 1960.
- [5] J. E. Warren and P. J. Root, “The behavior of naturally fractured reservoirs,” *Society of Petroleum Engineers Journal*, vol. 3, pp. 245–255, 1963.
- [6] S. Geiger, M. Dentz, and A. I. Neuweiler, “Novel multi-rate dual-porosity model for improved simulation of fractured and multiporosity reservoirs,” *SPE J.*, 0, vol. 4, pp. 670–684, 2013.
- [7] K. Ghorayeb and A. Firoozabadi, “Numerical study of natural convection and diffusion in fractured porous media,” *Spe Journal*, vol. 5, pp. 12–20, 2000.
- [8] J. Noorishad and M. Mehran, “An upstream finite element method for solution of transient transport equation in fractured porous media,” *Water Resources Research*, vol. 18, no. 3, pp. 588–596, 1982.
- [9] R. G. Baca, R. C. Arnett, and D. W. Langford, “Modelling fluid flow in fractured-porous rock masses by finite-element techniques,” *International Journal for Numerical Methods in Fluids*, vol. 4, no. 4, pp. 337–348, 1984.
- [10] J. G. Kim and M. D. Deo, *Comparison of the performance of a discrete fracture multiphase model with those using conventional methods*. In SPE Reservoir Simulation Symposium. Society of Petroleum Engineers, 1999, January.
- [11] J. G. Kim and M. D. Deo, “Finite element, discrete-fracture model for multiphase flow in porous media,” *AIChE Journal*, vol. 46, no. 6, pp. 1120–1130, 2000.
- [12] M. Karimi-Fard and A. Firoozabadi, “Numerical simulation of water injection in 2D fractured media using discrete-fracture model,” *Society of Petroleum Engineers*, 2001. In SPE annual technical conference and exhibition.
- [13] S. Geiger-Boschung, S. K. Matthäi, J. Niessner, and R. Helmig, “Black-oil simulations for three-component, three-phase flow in fractured porous media,” *SPE journal*, vol. 14, no. 02, pp. 338–354, 2009.
- [14] N. Zhang, J. Yao, Z. Huang, and Y. Wang, “Accurate multiscale finite element method for numerical simulation of two-phase flow in fractured media using discrete-fracture model,” *Journal of Computational Physics*, vol. 242, pp. 420–438, 2013.
- [15] L. Li and S. H. Lee, “Efficient field-scale simulation of black oil in a naturally fractured reservoir through discrete fracture networks and homogenized media,” *SPE Reservoir Evaluation & Engineering*, vol. 11, no. 04, pp. 750–758, 2008.
- [16] A. Moinfar, “Development of an efficient embedded discrete fracture model for 3D compositional reservoir simulation in fractured reservoirs,” 2013. Ph.D. Thesis, University of Texas, Austin.
- [17] X. Yan, Z. Huang, J. Yao, Y. Li, and D. Fan, “An efficient embedded discrete fracture model based on mimetic finite difference method,” *Journal of Petroleum Science and Engineering*, vol. 145, pp. 11–21, 2016.
- [18] M. Tene, S. Bosma, M. Al Kobaisi, and H. Hajibeygi, “Projection-based embedded discrete fracture model (pEDFM),” *Advances in Water Resources*, vol. 105, pp. 205–216, 2017.

- [19] J. Jiang and R. M. Younis, “An improved projection-based embedded discrete fracture model (pEDFM) for multiphase flow in fractured reservoirs,” *Advances in water resources*, vol. 109, pp. 267–289, 2017.
- [20] M. HosseiniMehr, M. Cusini, C. Vuik, and H. Hajibeygi, “Algebraic dynamic multilevel method for embedded discrete fracture model (F-ADM),” *Journal of Computational Physics*, vol. 373, pp. 324–345, 2018.
- [21] J. Xu, B. Sun, and B. Chen, “A hybrid embedded discrete fracture model for simulating tight porous media with complex fracture systems,” *Journal of Petroleum Science and Engineering*, vol. 174, pp. 131–143, 2019.
- [22] C. Alboin, J. Jaffré, J. Roberts, and C. Serres, “Domain decomposition for flow in porous media with fractures,” in *Domain Decomposition Methods in Sciences and Engineering* (M. C. C. H. Lai, P. E. Bjorstad, and O. Widlund, eds.), pp. 365–373, Domain Decomposition Press, Bergen, Norway: vol. 53, 1999.
- [23] C. Alboin, J. Jaffré, J. E. Roberts, X. Wang, and C. Serres, “Domain decomposition for some transmission problems in flow in porous media,” in *Numerical Treatment of Multiphase Flows in Porous Media*, pp. 22–34, Berlin: Springer, Heidelberg, 2000.
- [24] A. Hansbo and P. Hansbo, “An unfitted finite element method, based on nitsche’s method, for elliptic interface problems,” *Computer methods in applied mechanics and engineering*, vol. 191, no. 47–48, pp. 5537–5552, 2002.
- [25] L. H. Odsæter, T. Kvamsdal, and M. G. Larson, “A simple embedded discrete fracture–matrix model for a coupled flow and transport problem in porous media,” *Computer Methods in Applied Mechanics and Engineering*, vol. 343, pp. 572–601, 2019.
- [26] A. Fumagalli and A. Scotti, “An efficient XFEM approximation of Darcy flows in arbitrarily fractured porous media,” *Oil & Gas Science and Technology–Revue d’IFP Energies nouvelles*, vol. 69, no. 4, pp. 555–564, 2014.
- [27] H. Huang, T. A. Long, J. Wan, and W. P. Brown, “On the use of enriched finite element method to model subsurface features in porous media flow problems,” *Computational Geosciences*, vol. 15, no. 4, pp. 721–736, 2011.
- [28] N. Schwenck, “An XFEM-based model for fluid flow in fractured porous media,” 2015. Ph.D. Thesis, Universität Stuttgart.
- [29] S. Salimzadeh and N. Khalili, “Fully coupled XFEM model for flow and deformation in fractured porous media with explicit fracture flow,” *International Journal of Geomechanics*, vol. 16, no. 4, p. 04015091, 2015.
- [30] B. Flemisch, A. Fumagalli, and A. Scotti, “A review of the XFEM-based approximation of flow in fractured porous media,” in *Advances in Discretization Methods*, pp. 47–76, Springer, Cham., 2016.
- [31] M. Köppel, V. Martin, J. Jaffré, and J. E. Roberts, “A Lagrange multiplier method for a discrete fracture model for flow in porous media,” *Computational Geosciences*, vol. 23, no. 2, pp. 239–253, 2019.
- [32] M. Köppel, V. Martin, and J. E. Roberts, “A stabilized Lagrange multiplier finite-element method for flow in porous media with fractures,” *GEM-International Journal on Geomathematics*, vol. 10, 2019. Article number: 7 (2019).
- [33] P. Schädle, P. Zulian, D. Vogler, S. R. Bhopalam, M. G. Nestola, A. Ebigbo, R. Krause, and M. O. Saar, “3D non-conforming mesh model for flow in fractured porous media using Lagrange multipliers,” *Computers and Geosciences*, vol. 132, pp. 42–55, 2019.
- [34] J. E. P. Monteagudo and A. Firoozabadi, “Control-volume method for numerical simulation of two-phase immiscible flow in two-and three-dimensional discrete-fractured media,” *Water resources research*, vol. 40, p. W07405, 2004.
- [35] V. Reichenberger, H. Jakobs, P. Bastian, and R. Helmig, “A mixed-dimensional finite volume method for two-phase flow in fractured porous media,” *Advances in water resources*, vol. 29, no. 7, pp. 1020–1036, 2006.
- [36] J. E. Monteagudo and A. Firoozabadi, “Control-volume model for simulation of water injection in fractured media: incorporating matrix heterogeneity and reservoir wettability effects,” *SPE journal*, vol. 12, no. 03, pp. 355–366, 2007.
- [37] R. H. Zhang, L. H. Zhang, J. X. Luo, Z. D. Yang, and M. Y. Xu, “Numerical simulation of water flooding in natural fractured reservoirs based on control volume finite element method,” *Journal of Petroleum Science and Engineering*, vol. 146, pp. 1211–1225, 2016.
- [38] M. Karimi-Fard, L. J. Durlofsky, and K. Aziz, “An efficient discrete fracture model applicable for general purpose reservoir simulators,” in *SPE Reservoir Simulation Symposium. Society of Petroleum Engineers*, 2003.
- [39] T. H. Sandve, I. Berre, and J. M. Nordbotten, “An efficient multi-point flux approximation method for discrete fracture–matrix simulations,” *Journal of Computational Physics*, vol. 231, no. 9, pp. 3784–3800, 2012.
- [40] R. Ahmed, M. G. Edwards, S. Lamine, B. A. Huisman, and M. Pal, “Control-volume distributed multi-point flux approximation coupled with a lower-dimensional fracture model,” *Journal of Computational Physics*, vol. 284, pp. 462–489, 2015.
- [41] D. Gläser, R. Helmig, B. Flemisch, and H. Class, “A discrete fracture model for two-phase flow in fractured porous media,” *Advances in Water Resources*, vol. 110, pp. 335–348, 2017.
- [42] W. Fang, C. Liu, J. Li, H. Jiang, J. Pu, H. Gu, and X. Qin, “A discrete modeling framework for reservoirs with complex fractured media: Theory, validation and case studies,” *Journal of Petroleum Science and Engineering*, vol. 170, pp. 945–957, 2018.

- [43] H. Hoteit and A. Firoozabadi, “Multicomponent fluid flow by discontinuous Galerkin and mixed methods in unfractured and fractured media,” *Water Resources Research*, vol. 41, p. W11412, 2005.
- [44] H. Hoteit and A. Firoozabadi, “Compositional modeling of discrete-fractured media without transfer functions by the discontinuous Galerkin and mixed methods,” *SPE journal*, vol. 11, no. 03, pp. 341–352, 2006.
- [45] H. Hoteit and A. Firoozabadi, “Numerical modeling of two-phase flow in heterogeneous permeable media with different capillarity pressures,” *Advances in Water Resources*, vol. 31, no. 1, pp. 56–73, 2008.
- [46] H. Hoteit and A. Firoozabadi, “An efficient numerical model for incompressible two-phase flow in fractured media,” *Advances in Water Resources*, vol. 31, no. 6, pp. 891–905, 2008.
- [47] J. Moortgat and A. Firoozabadi, “Higher-order compositional modeling of three-phase flow in 3D fractured porous media based on cross-flow equilibrium,” *Journal of Computational Physics*, vol. 250, pp. 425–445, 2013.
- [48] J. B. Moortgat and A. Firoozabadi, “Three-phase compositional modeling with capillarity in heterogeneous and fractured media,” *SPE Journal*, vol. 18, no. 06, pp. 1–150, 2013.
- [49] A. Zidane and A. Firoozabadi, “An efficient numerical model for multicomponent compressible flow in fractured porous media,” *Advances in water resources*, vol. 74, pp. 127–147, 2014.
- [50] J. Moortgat, M. A. Amooie, and M. R. Soltanian, “Implicit finite volume and discontinuous Galerkin methods for multicomponent flow in unstructured 3D fractured porous media,” *Advances in water resources*, vol. 96, pp. 389–404, 2016.
- [51] P. F. Antonietti, C. Facciola, A. Russo, and M. Verani, “Discontinuous Galerkin approximation of flows in fractured porous media on polytopic grids,” *SIAM Journal on Scientific Computing*, vol. 41, no. 1, pp. A109–A138, 2019.
- [52] Z. Xu and Y. Yang, “The hybrid dimensional representation of permeability tensor: A reinterpretation of the discrete fracture model and its extension on nonconforming meshes,” *Journal of Computational Physics*, vol. 415, p. 109523, 2020.
- [53] W. Feng, H. Guo, Z. Xu, and Y. Yang, “Conservative numerical methods for the reinterpreted discrete fracture model on non-conforming meshes and their applications in contaminant transportation in fractured porous media,” *Advances in Water Resources*, vol. 153, p. 103951, 2021.
- [54] B. Flemisch, I. Berre, W. Boon, A. Fumagalli, N. Schwenck, A. Scotti, I. Stefansson, and A. Tatomir, “Benchmarks for single-phase flow in fractured porous media,” *Advances in Water Resources*, vol. 111, pp. 239–258, 2018.
- [55] E. Burman, P. Hansbo, M. G. Larson, and K. Larsson, “Cut finite elements for convection in fractured domains,” *Computers and Fluids*, vol. 179, pp. 726–734, 2019.
- [56] J. Jiang and R. M. Younis, “An improved projection-based embedded discrete fracture model (pEDFM) for multiphase flow in fractured reservoirs,” *Advances in water resources*, vol. 109, pp. 267–289, 2017.
- [57] O. Olorode, B. Wang, and H. U. Rashid, *Three-Dimensional Projection-Based Embedded Discrete-Fracture Model for Compositional Simulation of Fractured Reservoirs*. SPE Journal, 2020.
- [58] V. Martin, J. Jaffré, and J. E. Roberts, “Modeling fractures and barriers as interfaces for flow in porous media,” *SIAM Journal on Scientific Computing*, vol. 26, no. 5, pp. 1667–1691, 2005.
- [59] P. Angot, F. Boyer, and F. Hubert, “Asymptotic and numerical modelling of flows in fractured porous media,” *ESAIM: Mathematical Modelling and Numerical Analysis*, vol. 43, no. 2, pp. 239–275, 2009.
- [60] W. Boon, J. Nordbotten, and I. Yotov, “Robust discretization of flow in fractured porous media,” *SIAM Journal on Numerical Analysis*, vol. 56, pp. 2203–2233, 2018.
- [61] T. Kadeethum, H. Nick, S. Lee, and F. Ballarin, “Flow in porous media with low dimensional fractures by employing enriched galerkin method,” *Advances in Water Resources*, vol. 142, p. 103620, 2020.
- [62] Z. Xu, Z. Huang, and Y. Yang, “The Hybrid-dimensional Darcy’s Law: A Reinterpreted Discrete Fracture Model for Fracture and Barrier Networks on Non-conforming Meshes,” 2021.
- [63] C. Alboin, J. Jaffré, J. Roberts, and C. Serres, “Modeling fractures as interfaces for flow and transport in porous media,” in *Fluid flow and transport in porous media: mathematical and numerical treatment (South Hadley, MA, 2001)*, vol. 295 of *Contemp. Math.*, pp. 13–24, Amer. Math. Soc., Providence, RI, 2002.
- [64] A. Fumagalli and A. Scotti, “A reduced model for flow and transport in fractured porous media with non-matching grids,” in *Numerical mathematics and advanced applications 2011*, pp. 499–507, Springer, Heidelberg, 2013.
- [65] F. Ilinca and J.-F. Héty, “A finite element immersed boundary method for fluid flow around rigid objects,” *Internat. J. Numer. Methods Fluids*, vol. 65, no. 7, pp. 856–875, 2011.
- [66] S. Frei and T. Richter, “A locally modified parametric finite element method for interface problems,” *SIAM J. Numer. Anal.*, vol. 52, no. 5, pp. 2315–2334, 2014.
- [67] F. Auricchio, F. Brezzi, A. Lefieux, and A. Reali, “An “immersed” finite element method based on a locally anisotropic remeshing for the incompressible Stokes problem,” *Comput. Methods Appl. Mech. Engrg.*, vol. 294, pp. 428–448, 2015.

- [68] L. Chen, H. Wei, and M. Wen, “An interface-fitted mesh generator and virtual element methods for elliptic interface problems,” *J. Comput. Phys.*, vol. 334, pp. 327–348, 2017.
- [69] I. Berre, W. Boon, B. Flemisch, A. Fumagalli, D. Gläser, E. Keilegavlen, A. Scotti, I. Stefansson, A. Tatomir, K. Brenner, S. Burbulla, P. Devloo, O. Duran, M. Favino, J. Hennicker, I.-H. Lee, K. Lipnikov, R. Masson, K. Mosthaf, M. C. Nestola, C.-F. Ni, K. Nikitin, P. Schädle, D. Svyatskiy, R. Yanbarisov, and P. Zulian, “Verification benchmarks for single-phase flow in three-dimensional fractured porous media,” *Advances in Water Resources*, vol. 147, p. 103759, 2021.
- [70] E. Keilegavlen, R. Berge, A. Fumagalli, M. Starnoni, I. Stefansson, J. Varela, and I. Berre, “PorePy: an open-source software for simulation of multiphysics processes in fractured porous media,” *Comput. Geosci.*, vol. 25, no. 1, pp. 243–265, 2021.
- [71] J. M. Nordbotten, W. M. Boon, A. Fumagalli, and E. Keilegavlen, “Unified approach to discretization of flow in fractured porous media,” *Comput. Geosci.*, vol. 23, no. 2, pp. 225–237, 2019.
- [72] B. Flemisch, M. Darcis, K. Erbertseder, B. Faigle, A. Lauser, K. Mosthaf, S. Müthing, P. Nuske, A. Tatomir, M. Wolff, and R. Helmig, “Dumux: Dune for multi-phase,component,scale,physics,... flow and transport in porous media,” *Advances in Water Resources*, vol. 34, no. 9, pp. 1102–1112, 2011. New Computational Methods and Software Tools.
- [73] K. Lipnikov, G. Manzini, and M. Shashkov, “Mimetic finite difference method,” *J. Comput. Phys.*, vol. 257, no. part B, pp. 1163–1227, 2014.
- [74] K. Brenner, J. Hennicker, R. Masson, and P. Samier, “Gradient discretization of hybrid-dimensional Darcy flow in fractured porous media with discontinuous pressures at matrix-fracture interfaces,” *IMA J. Numer. Anal.*, vol. 37, no. 3, pp. 1551–1585, 2017.
- [75] K. D. Nikitin and R. M. Yanbarisov, “Monotone embedded discrete fractures method for flows in porous media,” *J. Comput. Appl. Math.*, vol. 364, pp. 112353, 15, 2020.
- [76] J. Schöberl, “C++11 Implementation of Finite Elements in NGSolve,” 2014. ASC Report 30/2014, Institute for Analysis and Scientific Computing, Vienna University of Technology.
- [77] S. N. P. I. (SKI), “The international hydrocoin project- background and results. Paris, France: Organization for Economic Co-operation and Development,” 1987.
- [78] P.-A. Raviart and J. M. Thomas, “A mixed finite element method for 2nd order elliptic problems,” in *Mathematical aspects of finite element methods (Proc. Conf., Consiglio Naz. delle Ricerche (C.N.R.), Rome, 1975)*, pp. 292–315. Lecture Notes in Math., Vol. 606, 1977.
- [79] D. N. Arnold and F. Brezzi, “Mixed and nonconforming finite element methods: implementation, postprocessing and error estimates,” *RAIRO Modél. Math. Anal. Numér.*, vol. 19, no. 1, pp. 7–32, 1985.

DEPARTMENT OF APPLIED AND COMPUTATIONAL MATHEMATICS AND STATISTICS, UNIVERSITY OF NOTRE DAME, USA.

Email address: gfu@nd.edu

DEPARTMENT OF MATHEMATICAL SCIENCES, MICHIGAN TECHNOLOGICAL UNIVERSITY, USA.

Email address: yyang7@mtu.edu